Chaos

Complex bursting dynamics in an embryonic respiratory neuron model

Cite as: Chaos **30**, 043127 (2020); https://doi.org/10.1063/1.5138993
Submitted: 16 November 2019 . Accepted: 23 March 2020 . Published Online: 20 April 2020

Yangyang Wang, and Jonathan E. Rubin

Complex bursting dynamics in an embryonic respiratory neuron model

Cite as: Chaos **30**, 043127 (2020); doi: 10.1063/1.5138993
Submitted: 16 November 2019 · Accepted: 23 March 2020 ·
Published Online: 20 April 2020

Yangyang Wang[1,a)] and Jonathan E. Rubin[2,b)]

AFFILIATIONS

[1]Department of Mathematics, The University of Iowa, Iowa City, Iowa 52242, USA
[2]Department of Mathematics, University of Pittsburgh, Pittsburgh, Pennsylvania 15260, USA

[a)]**Electronic mail:** yangyang-wang@uiowa.edu
[b)]**Author to whom correspondence should be addressed:** jonrubin@pitt.edu

ABSTRACT

Pre-Bötzinger complex (pre-BötC) network activity within the mammalian brainstem controls the inspiratory phase of the respiratory rhythm. While bursting in pre-BötC neurons during the postnatal period has been extensively studied, less is known regarding inspiratory pacemaker neuron behavior at embryonic stages. Recent data in mouse embryo brainstem slices have revealed the existence of a variety of bursting activity patterns depending on distinct combinations of burst-generating I_{NaP} and I_{CAN} conductances. In this work, we consider a model of an isolated embryonic pre-BötC neuron featuring two distinct bursting mechanisms. We use methods of dynamical systems theory, such as phase plane analysis, fast–slow decomposition, and bifurcation analysis, to uncover mechanisms underlying several different types of intrinsic bursting dynamics observed experimentally including several forms of plateau bursts, bursts involving depolarization block, and various combinations of these patterns. Our analysis also yields predictions about how changes in the balance of the two bursting mechanisms contribute to alterations in an inspiratory pacemaker neuron activity during prenatal development.

A network of neurons in the mammalian brainstem controls breathing by sending electrical signals to the muscles involved. Within this network, certain neurons have pacemaker properties in the sense that they can drive a rhythmic network activity without receiving a patterned synaptic input from another source. Recent data show that the embryonic mouse brainstem already has respiratory pacemaker neurons, and their bursting properties are still under development shortly before birth. In this paper, by applying dynamical system methods to a model of an isolated embryonic respiratory neuron, we uncover the intrinsic rhythmogenic mechanisms underlying complex bursting patterns observed at embryonic stages. This analysis involves the study of the interaction of a variety of bifurcation mechanisms in the context of multiple timescale decompositions. We also consider how transitions between different bursting solutions that occur as model parameters vary in order to understand developmental changes in the patterns and mechanisms of respiratory pacemaker neuron dynamics.

I. INTRODUCTION

Breathing is a critical rhythmic behavior that continues from before birth up until death. It is generated by neuronal circuitry, including the pre-Bötzinger complex (pre-BötC),[35] which has been established to be critical for driving inspiration (reviewed in Refs. 5, 10, 15, 17, and 36, for example). Certain neurons in the pre-BötC can produce an intrinsic bursting activity in the absence of a synaptic input and hence represent natural candidates for performing a pacemaker function. Although this intrinsic bursting may become masked when the pre-BötC is embedded in the full respiratory network, this bursting capability nonetheless contributes to the network's rhythm generation properties.[31] Experimental recordings in postnatal rodent medullary slices containing pre-BötC have identified two bursting mechanisms depending on persistent sodium current (I_{NaP}) and a calcium-activated nonspecific cation current (I_{CAN}).[5,10,15,17]

These experimental observations have attracted the attention of computational researchers interested in using mathematical modeling to understand the cellular mechanisms for an intrinsic rhythmic bursting activity in the postnatal pre-BötC. Butera *et al.* developed and analyzed an early and influential computational model of isolated pre-BötC neurons, which produces bursting that depends on I_{NaP}. This bursting is part of a larger class of bursting patterns sometimes called *plateau bursting*, which feature active phases of sustained spiking riding on top of a voltage depolarization (the plateau). Later, a computational model of pre-BötC bursting dynamics based

on synaptic activation of I_{CAN} was developed,[30] which produced burst patterns in which active phases combined spiking periods together with periods of depolarization block (i.e., elevated voltage without spikes and associated synaptic transmission). Subsequent work combined burst mechanisms based on I_{NaP} and those based on I_{CAN} into a two-compartment pre-BötC neuron model (TB model) that produces three types of plateau bursting: I_{NaP}-*dependent* (*N*) *bursting*, I_{CAN}-*dependent* (*C*) *bursting*, and $I_{NaP} + I_{CAN}$-*dependent* (N + C) *bursting* that depends on both currents.[39] Similar bursting dynamics also arises in a reduced single-compartment model[8,22] derived from the TB model. Within this model, recent analysis has explained how the two bursting mechanisms interact to produce an irregular N + C bursting solution that consists of a sequence of short bursts separated by long bursts.[42] Such a mixed long/short bursting pattern is also seen in experimental recordings and other pre-BötC modeling work (e.g., Refs. 11 and 40), but it involves a rather different mechanism (see the discussion in Ref. 43).

While bursting dynamics in the postnatal pre-BötC has been extensively studied both experimentally and computationally, little is known regarding pre-BötC pacemaker neurons at embryonic stages and how they develop prior to birth. Chevalier *et al.* aimed to bridge this knowledge gap by providing the first description of intrinsic bursting properties in embryonic pre-BötC neurons, which depend on I_{NaP} and I_{CAN}. Specifically, three different discharge patterns were observed in embryonic pre-BötC pacemaker neurons: first, a plateau bursting pattern that closely resembles the discharge patterns expressed by postnatal pre-BötC neurons; second, a new bursting pattern involving a sustained depolarization block (DB); and a third, mixed bursting pattern that appears to represent a combination of these other two. Such heterogeneity of bursting patterns was shown to be associated with distinct combinations of the burst-generating NaP and CAN conductances. Indeed, experiments by Chevalier *et al.* indicate that DB bursting is sensitive to blockade of I_{CAN}, plateau bursting is affected by modulation of I_{NaP}, and changes in both currents alter properties of mixed bursting.

This observation raised the question of whether developmental alterations in the properties of pre-BötC bursting required replacement of I_{CAN}-expressing neurons, through cell death or silencing, with I_{NaP}-dominated neurons, or whether changes in burst patterns could result from modulation of NaP and CAN conductances within individual neurons across the prenatal period. To test the second possibility, Chevalier *et al.* developed an updated single-compartment model that encompasses both I_{NaP}-dependent and I_{CAN}-dependent bursting. This model can produce all three types of bursting solutions observed in embryonic pre-BötC neurons, depending on parameter tuning. Simulation results show that changing the proportion of NaP and CAN conductances within individual model pre-BötC neurons based on the actual changes of conductance proportions measured during embryonic development reproduces the progression of embryonic pre-BötC dynamics observed experimentally. This finding suggests that the developmental process underlying different pacemaker types at different embryonic stages could be a direct result of a switch in the relative proportions of I_{NaP} and I_{CAN} within individual neurons.

In this paper, we link past analysis of I_{NaP}-dependent, I_{CAN}-dependent, and $I_{NaP} + I_{CAN}$-dependent bursting dynamics in pre-BötC neurons[22,39,42,43] with a new analysis of DB and mixed plateau/DB bursting observed in embryonic stages to understand the full range of dynamics encoded within the embryonic pre-BötC neuron model from a mechanistic, dynamical systems perspective. This approach allows us to elucidate which model components conspire to produce which dynamic features, and how multiple timescales in the model contribute to the emergent dynamics. We also consider how the transitions between different activity patterns occur as parameters (NaP and CAN conductances) are varied, in order to gain a more precise understanding of the developmental changes needed to induce an effective transition in pre-BötC dynamics during the prenatal period. From a mathematical perspective, the key novel feature of this paper is a thorough analysis of mixed bursting dynamics that includes repeatedly alternating N, DB, and N + C bursts. Although this pattern arises on a relatively limited parameter region, it is the critical form of dynamics for understanding what factors, on each cycle, determine which type of burst emerges. Once we explain this core selection mechanism, we can understand how parameter changes move the model between regimes with different types of bursting represented, which is a key point for how pre-BötC neuron dynamics evolves developmentally.

The remainder of the paper is organized as follows. The single-compartment embryonic pre-BötC neuron model developed in Ref. 4 is described in Sec. II. In Sec. III, we discuss a classification of bursting types in this model that are characterized by different values of the conductances g_{NaP} and g_{CAN}. Section IV uses a bifurcation analysis to uncover the mechanisms underlying the three bursting patterns that were observed in experimental recordings. In Sec. V, we investigate how variations of the CAN and NaP conductances induce transitions between different activity patterns in the model. The paper ends with a discussion in Sec. VI.

II. MODEL

Following past work,[39,40] Chevalier *et al.* proposed an embryonic pre-BötC neuron model that includes key experimentally identified voltage-gated currents as well as intracellular calcium dynamics. The dynamics of this model is given by the following equations:

$$\begin{aligned}
C_m \frac{dV}{dt} &= -I_{NaP} - I_{Na} - I_K - I_{Ca} - I_{CAN} - I_L,\\
\frac{dn}{dt} &= (n_\infty(V) - n)/\tau_n,\\
\frac{dh}{dt} &= (h_\infty(V) - h)/\tau_h,\\
\frac{d\mathrm{Ca_i}}{dt} &= \frac{f_i}{V_i}\left(\frac{1}{\lambda}(J_{PMin} - J_{PMout}) + (J_{ERin} - J_{ERout})\right),\\
\frac{d\mathrm{Ca_{tot}}}{dt} &= \frac{f_i}{V_i}\left(\frac{1}{\lambda}(J_{PMin} - J_{PMout})\right),\\
\frac{dl}{dt} &= A(K_d - l(\mathrm{Ca_i} + K_d)),
\end{aligned} \tag{1}$$

with currents

$$\begin{aligned} I_{\mathrm{NaP}} &= g_{\mathrm{NaP}} m p_\infty(V) h (V - V_{\mathrm{Na}}), \\ I_{\mathrm{Na}} &= g_{\mathrm{Na}} m_\infty^3(V)(1-n)(V - V_{\mathrm{Na}}), \\ I_{\mathrm{K}} &= g_{\mathrm{K}} n^4 (V - V_{\mathrm{K}}), \\ I_{\mathrm{Ca}} &= g_{\mathrm{Ca}} m p_\infty(V)(V - V_{\mathrm{Ca}}), \\ I_{\mathrm{CAN}} &= g_{\mathrm{CAN}} \mathrm{CAN}_\infty(\mathrm{Ca}_i)(V - V_{\mathrm{Na}}), \\ I_{\mathrm{L}} &= g_{\mathrm{L}}(V - V_{\mathrm{L}}), \end{aligned} \tag{2}$$

additional kinetic functions

$$\begin{aligned} x_\infty &= \frac{1}{1 + \exp((V - V_x)/s_x)}, \quad x \in \{mp, m, n, h\}, \\ \tau_y &= \bar{\tau}_y / \cosh((V - V_y)/2s_y), \quad y \in \{n, h\}, \\ \mathrm{CAN}_\infty(\mathrm{Ca_i}) &= \frac{\mathrm{Ca_i}}{\mathrm{Ca_i} + \mathrm{K_{CAN}}}, \end{aligned} \tag{3}$$

and calcium-related terms

$$\begin{aligned} J_{\mathrm{PMin}} &= -\alpha I_{\mathrm{Ca}}, \\ J_{\mathrm{PMout}} &= V_{\mathrm{PMCA}} \frac{\mathrm{Ca_i^2}}{K_{\mathrm{PMCA}}^2 + \mathrm{Ca_i^2}}, \\ J_{\mathrm{ERin}} &= \left(L_{\mathrm{IP_3}} + P_{\mathrm{IP_3}} \left[\frac{[\mathrm{IP_3}]\mathrm{Ca_i} l}{([\mathrm{IP_3}] + K_{\mathrm{I}})(\mathrm{Ca_i} + K_a)} \right]^3 \right) (\mathrm{Ca_{ER}} - \mathrm{Ca_i}), \\ \mathrm{Ca_{ER}} &= \frac{\mathrm{Ca_{tot}} - \mathrm{Ca_i}}{\sigma}, \\ J_{\mathrm{ERout}} &= V_{\mathrm{SERCA}} \frac{\mathrm{Ca_i^2}}{K_{\mathrm{SERCA}}^2 + \mathrm{Ca_i^2}}. \end{aligned} \tag{4}$$

The model (1)–(4) describes the evolution of voltage V, the voltage-dependent gating variables n, h, and calcium-related variables. For the former group, model dimensionality is reduced using the standard steps of treating sodium activation as instantaneous and imposing a linear relation between the inactivating of the fast (i.e., not persistent) sodium current and the activation of the potassium current, based on the nearly linear path that spiking trajectories trace out when projected to the space of these two gating variables in the full Hodgkin–Huxley model.[14,27] To reduce the number of parameters, the activation of I_{Ca} was chosen to be the same as the activation function mp_∞ for I_{NaP}, as in previous models,[4,40] and we also followed past work[22,39,40] in setting the reversal potential of I_{CAN} equal to V_{Na}, reflecting a dominant sodium contribution to this current. The calcium-related variables comprise the intracellular calcium concentration $\mathrm{Ca_i}$, the combined intracellular and endoplasmic reticulum (ER) calcium concentration $\mathrm{Ca_{tot}}$, and the fraction l of $\mathrm{IP_3}$ channels that have not been inactivated, which modulates the flux of calcium between the ER and cytosol. In addition to $\mathrm{IP_3}$, the calcium dynamics depend on the activity of SERCA and plasma membrane (PMCA) pumps. In this paper, we call (V, n, h) the *voltage* subsystem and $(\mathrm{Ca_i}, \mathrm{Ca_{tot}}, l)$ the *calcium* subsystem. Values for parameters other than g_{NaP}, g_{CAN} are given in Table I; for additional details on the biology underlying the model, see Refs. 4, 22, and 39. Note that when $[\mathrm{IP_3}] = 1$, $\mathrm{Ca_i}$ in the calcium subsystem oscillates.

III. SIMULATION RESULTS

Past works[22,39,42] have shown that the model (1)–(4) can produce dynamically different bursting behaviors as values of the conductances $g_{\mathrm{NaP}}, g_{\mathrm{CAN}}$ are varied. When there are no Ca^{2+} oscillations and persistent sodium is in the bursting range, where I_{NaP} alternates between activation and inactivation, we refer to the bursting as I_{NaP}-*dependent* (N) bursting. However, for parameters given in Table I, the model (1)–(4) produces Ca^{2+} oscillations. Hence, in this work, N bursting only occurs when $g_{\mathrm{CAN}} = 0$ nS so that the system is independent of calcium oscillations and g_{NaP} is in the bursting range. When $g_{\mathrm{CAN}} \neq 0$ nS and g_{NaP} is in the sub-oscillatory range where I_{NaP} is not activated, we refer to the bursting relying only on I_{CAN} as I_{CAN}-*dependent* (C) bursting. When $g_{\mathrm{CAN}} \neq 0$ nS and g_{NaP} is in the oscillatory bursting range, we refer to bursting that features a jump in $\mathrm{Ca_i}$ as $I_{\mathrm{NaP}} + I_{\mathrm{CAN}}$-*dependent* (N + C) bursting. As noted in Sec. I, all of these burst types are referred to as *plateau bursting*.

TABLE I. The parameter values for the model (1)–(4).

Parameters related to	
I_{NaP}	$V_h = -48$ mV; $V_{mp} = -40$ mV; $s_{mp} = -6$ mV; $s_h = 5$ mV; $\bar{\tau}_h = 10\,000$ ms;
I_{Na}	$g_{\mathrm{Na}} = 28$ nS; $V_m = -34$ mV; $V_n = -29$ mV; $s_m = -5$ mV; $s_n = -4$ mV; $\bar{\tau}_n = 10$ ms; $V_{\mathrm{Na}} = 50$ mV
I_{K}	$g_{\mathrm{K}} = 11.2$ nS; $V_{\mathrm{K}} = -65$ mV
I_{Ca}	$g_{\mathrm{Ca}} = 0.05$ nS; $V_{\mathrm{Ca}} = 150$ mV; $\alpha = 0.055\ \mu$M/fC; $V_{\mathrm{PMCA}} = 2\ \mu$M/ms; $K_{\mathrm{PMCA}} = 0.3\ \mu$M
I_{CAN}	$K_{\mathrm{CAN}} = 0.74\ \mu$M
I_{L}	$g_{\mathrm{L}} = 2.7$ nS; $V_{\mathrm{L}} = -60$ mV
ER Ca	$\lambda = 0.04$; $f_i = 0.0001$; $V_i = 4$; $[\mathrm{IP_3}] = 1\ \mu$M; $A = 0.0005\ \mu$M/ms; $V_{\mathrm{SERCA}} = 400\ \mu$M/ms; $K_{\mathrm{SERCA}} = 0.2\ \mu$M; $\sigma = 0.185$; $L_{\mathrm{IP_3}} = 0.37$/ms; $P_{\mathrm{IP_3}} = 31\,000$ /ms; $\mathrm{K_I} = 1\ \mu$M; $\mathrm{K_d} = 0.4\ \mu$M; $\mathrm{K_a} = 0.4\ \mu$M
Other	$C_m = 21$ pF

TABLE II. Example parameter values supporting each burst type.

Bursting type	(V, n, h) behavior	Coupling from Ca_i
I_{NaP}-dependent	$g_{NaP} = 2.5$ nS	$g_{CAN} = 0$ nS
I_{CAN}-dependent	$g_{NaP} = 1$ nS	$g_{CAN} = 1$ nS
Depolarization block	$g_{NaP} = 2.5$ nS	$g_{CAN} = 2.5$ nS
I_{NaP}-dependent/$I_{NaP} + I_{CAN}$-dependent	$g_{NaP} = 4$ nS	$g_{CAN} = 0.5$ nS
I_{NaP}-dependent/depolarization block	$g_{NaP} = 4$ nS	$g_{CAN} = 2$ nS
Mixed (I_{NaP}-dependent/depolarization block/$I_{NaP} + I_{CAN}$-dependent)	$g_{NaP} = 2.5$ nS	$g_{CAN} = 1$ nS

Alternatively, bursting with a group of rapid spikes followed by a depolarized silence is referred as *depolarization block* (DB) bursting. These bursting behaviors can also occur in various combinations for fixed parameter values. Examples of these bursting types and parameter values used to obtain them are given in Table II and Fig. 1.

When the voltage subsystem decouples from the calcium dynamics at $g_{CAN} = 0$ nS, increasing g_{NaP} leads to the transition from silence to N bursting. When g_{CAN} is relatively small, the increase of g_{NaP} causes the transition from silence to N + C bursting [Fig. 1(a), gray shaded area in the lower left corner; e.g., when $g_{NaP} = 2$ nS, $g_{CAN} = 0.5$ nS] to I_{NaP}-dependent/$I_{NaP} + I_{CAN}$-dependent (N/N +

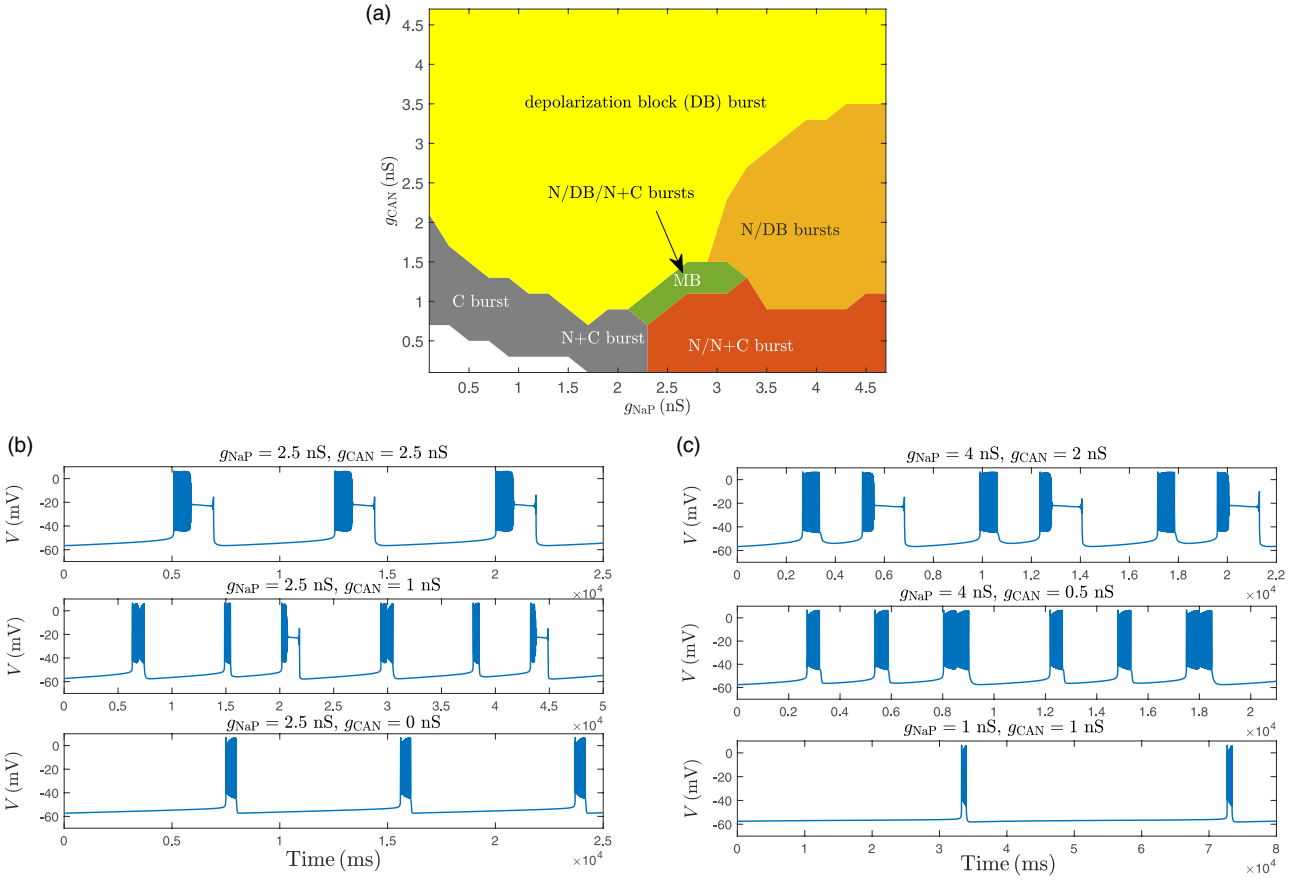

FIG. 1. The type of bursting activity is determined by parameter values g_{NaP} and g_{CAN}. (a) The range of g_{NaP} and g_{CAN} for different types of activity patterns in the model (1)–(4). White color represents silence, and other colors are bursting. (b) For $g_{NaP} = 2.5$ nS, the model neuron generates a DB bursting discharge ($g_{CAN} = 2.5$ nS, top); a mixed bursting pattern consisting of I_{NaP}-dependent (N), DB, and $I_{NaP} + I_{CAN}$-dependent (N + C) bursting types ($g_{CAN} = 1$ nS, middle); and an N bursting pattern ($g_{CAN} = 0$ nS, bottom). (c) For $g_{NaP} = 4$ nS, the model neuron generates mixed bursting patterns consisting of N and DB bursting ($g_{CAN} = 2$ nS, top) and solution patterns consisting of N and N + C bursting ($g_{CAN} = 0.5$ nS, middle). When $g_{NaP} = g_{CAN} = 1$ nS, an I_{CAN}-dependent (C) bursting pattern is produced (bottom); note the elongated time axis in the bottom panel. All patterns repeat periodically.

C) bursting consisting of a sequence of N bursts followed by a N + C burst [Fig. 1(a), red shaded area in the lower right corner; Fig. 1(c) middle panel]. Starting from the red region with N/N + C bursting solutions for which the voltage compartment is itself burst-capable at low Ca_i and transits to the long (N + C) burst as Ca_i jumps up, the increase of g_{CAN} leads to the transition from N/N + C bursting to I_{NaP}-dependent/depolarization block (N/DB) bursting and eventually to pure DB bursting. This transition occurs because calcium oscillations contribute more and more significantly to a sustained shift in the membrane potential as g_{CAN} increases. Figure 1 also implies that for any g_{NaP}, a large enough value of g_{CAN} always leads to a DB bursting solution. Notice that although Fig. 1 does not cover the regime where g_{NaP} is large, it follows from Ref. 42 that bursting dynamics in the voltage subsystem will eventually give way to tonic spiking for large enough g_{NaP}. Recall that the model (1)–(4) always exhibits Ca^{2+} oscillations. Hence, a transition from N/N + C [Fig. 1(a), red shaded area] to N + C dynamics for g_{CAN} relatively small or a transition from N/DB [Fig. 1(a), orange shaded area] to DB bursting for intermediate g_{CAN} values will occur as g_{NaP} becomes large enough.

Last, a *mixed bursting* (MB) pattern that consists of alternating I_{NaP}-dependent, DB, and $I_{NaP} + I_{CAN}$-*dependent* bursts exists in a small green region in Fig. 1(a) [see also the middle panel of Fig. 1(b)]. Such mixed bursting solutions have sensitive dependence to g_{NaP} and g_{CAN}, a small change of which can lead to the transition from mixed bursting to C, N/N + C, N/DB, or DB bursts in the full model. Mathematically, this parameter sensitivity is suggestive of an organizing center of the model dynamics in the parameter space.

IV. BIFURCATION ANALYSIS

Our analysis depends on exploiting the presence of different timescales. As a first step, we rescale the variables to explicitly identify the important timescales. We define new dimensionless variables (v, c, c_{tot}, τ) and voltage, calcium, and time scales Q_v, Q_c, and Q_t, respectively, such that

$$V = Q_v \cdot v, \quad Ca_i = Q_c \cdot c, \quad Ca_{tot} = Q_c \cdot c_{tot}, \quad t = Q_t \cdot \tau.$$

Note that n, h, and l are already dimensionless in (1).

Details of the nondimensionalization procedure, including the determination of appropriate values for Q_v, Q_c, Q_t, are given in the Appendix. From this process, we obtain a dimensionless system of the form

$$\begin{aligned} R_v \frac{dv}{d\tau} &=: f_1(v, n, h, c), \\ R_n \frac{dn}{d\tau} &=: g_1(v, n), \\ R_h \frac{dh}{d\tau} &=: h_1(v, h), \\ R_c \frac{dc}{d\tau} &=: f_2(v, c, c_{tot}, l), \\ R_{c_{tot}} \frac{dc_{tot}}{d\tau} &=: g_2(v, c), \\ R_l \frac{dl}{d\tau} &=: h_2(c, l), \end{aligned} \tag{5}$$

where R_* are given in (A3) in the Appendix. Timescales of the variables in (1) are summarized in Table III.

This nondimensionalization result suggests that V, n evolve on a fast timescale, Ca_i evolves on a slow timescale, and h, Ca_{tot}, l evolve on a superslow timescale. The voltage subsystem (V, n, h) is, therefore, a fast–slow subsystem and the calcium subsystem (Ca_i, Ca_{tot}, l) is a slow–superslow subsystem. To analyze the dynamics of model (1)–(4), we follow Refs. 42 and 43 to first use fast–slow decomposition to study the voltage subsystem and then consider the effect of the calcium subsystem on the resulting bifurcation diagram by using 2-parameter bifurcation diagrams. In order to understand the mixed bursting solution that consists of three different types of bursting, we go beyond a traditional fast–slow decomposition by considering the competition between rates of changes of Ca_i and h in different regions of the phase space (see Sec. IV C).

In the following, we use a bifurcation analysis to illustrate the underlying mechanisms of the I_{NaP}-dependent bursting pattern occurring when $g_{NaP} = 2.5$ nS, $g_{CAN} = 0$ nS [Fig. 1(b), bottom panel] in Sec. IV A, the depolarization block bursting pattern when $g_{NaP} = 2.5$ nS, $g_{CAN} = 2.5$ nS [Fig. 1(b), top panel] in Sec. IV B, and the mixed bursting pattern arising when $g_{NaP} = 2.5$ nS, $g_{CAN} = 1$ nS [Fig. 1(b), middle panel] in Sec. IV C.

A. Bifurcation analysis for the I_{NaP}-dependent bursting solution

Since the (V, n, h) subsystem decouples from the calcium dynamics when g_{CAN} is 0, we can determine the mechanisms underlying I_{NaP}-dependent bursting directly from the bifurcation diagram of the (V, n, h) system as shown in Fig. 2. Fast–slow decomposition analysis can be performed by treating the slow variable h as a bifurcation parameter for the fast subsystem encompassing the dynamics of the remaining variables (V, n). The resulting bifurcation diagram (Fig. 2, right) includes an S-shaped curve of equilibria (S) and a family of stable periodic orbits (P) for the (V, n) system. In fact, an unstable family of periodic orbits emanates from S in an Andronov–Hopf bifurcation (HB), and this family meets P in a saddle node of periodic orbits bifurcation (SNPO). P exists for h values below this SNPO, down to a minimal value where P terminates in a homoclinic bifurcation (HC). S itself turns around at two *saddle-node* or *fold* bifurcations. This structure shows that the

TABLE III. Timescales for the model (1).

V	n	h	Ca_i	Ca_{tot}	l
$O(1)$ ms	$O(0.1)$ ms	$O(1000)$ ms	$O(10)$ ms	$O(1000)$ ms	$O(1000)$ ms

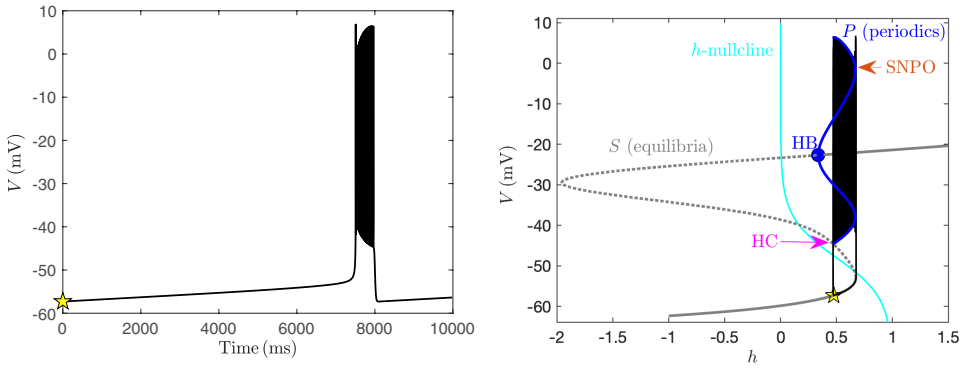

FIG. 2. The I_{NaP}-dependent bursting solution produced by the system (1)–(4) when $g_{CAN} = 0$ nS, $g_{NaP} = 2.5$ nS. Left: Voltage time series for one burst cycle. Right: Projection onto the (h, V)-space of the burst trajectory (black) shown in the left panel and the bifurcation diagram for the fast (V, n) subsystem with respect to h, along with the h-nullcline shown in cyan. The S-shaped curve (S) (grey; solid where attracting, dashed otherwise) denotes the fixed points of the V, n equations in (1) with h taken as a constant parameter, and the blue curve shows the maximum and minimum V along two families of periodic orbits, an unstable one born at the subcritical Andronov–Hopf bifurcation (HB, blue dot) and a stable one (P) that coalesces with the unstable one at a saddle node of periodic orbits (SNPO) bifurcation. HC denotes a homoclinic bifurcation in which P terminates. The curve S intersects the h-nullcline at three unstable fixed points of the full model (1).

fast subsystem (V, n) has three possible stable states: a low voltage equilibrium state that extends over a wide range of h values, a high voltage equilibrium state that exists for large enough h, and an oscillatory state that overlaps with the other two. Next, we impose the slow dynamics on top of this fast subsystem structure to understand the full system behavior that emerges in this parameter regime.

Consider the position of the h-nullcline in relation to the fast subsystem bifurcation diagram. The lowest intersection point lies in the middle branch of S, yet at an h value below the HC bifurcation; hence, the I_{NaP}-dependent bursting that the system exhibits is in fact a square-wave bursting solution, consisting of a slow drift to the right along the lower branch of S, a fast jump to the periodic orbit branch P at the lower fold of S, fast oscillations along P accompanied by a slow drift to the left in h, and a fast jump back down to the lower branch of S near HC on each cycle.

B. Bifurcation analysis for the depolarization block (DB) bursting solution

When $g_{NaP} = g_{CAN} = 2.5$ nS, system (1) features a bidirectional coupling between V and Ca_i and produces DB bursting dynamics [Fig. 3(a)]. We explain the underlying mechanisms from the perspective of how the voltage subsystem (V, n, h) is driven by the calcium subsystem (Ca_i, Ca_{tot}, l). The analysis should proceed in three steps: (1) investigate the I_{NaP}-based mechanism underlying the continuous spiking in black generated by the voltage subsystem through a bifurcation analysis, (2) explore the transition from spiking to the DB by studying the effect of the calcium subsystem on the resulting bifurcation structures, and (3) study the calcium dynamics produced by the calcium subsystem by considering how it is impacted by voltage. We point to Sec. IV A for the analysis in step (1) and only illustrate our results for steps (2) and (3).

Note from Eq. (2) that g_{CAN} multiplies an increasing function of Ca_i. Hence, although g_{CAN} is now larger than in Sec. IV A, for small Ca_i, the bifurcation diagram of the (V, n) fast subsystem with respect to h is the same as in Fig. 2, right. Due to the coupling effect of Ca_i on the voltage subsystem, increasing Ca_i moves S and P to smaller h values. Figure 3(c) shows specific examples with Ca_i at its minimum (gray) and maximum (blue) observed over a DB burst cycle, while Fig. 3(d) shows how the key bifurcation points in this diagram vary with continuous variation of Ca_i. Note that as Ca_i increases toward about $Ca_i = 0.1\ \mu$M, the SN curve meets the HC curve, corresponding to a switch in the termination of the stable periodic orbit family P from a standard HC bifurcation to a saddle node on an invariant circle (SNIC) bifurcation [although for simplicity, we maintain the HC label in Fig. 3(d)].

Given these effects, we can now consider the dynamics of the full system when h and the calcium variables evolve along with V and n. The four panels of Fig. 3 show different views of a DB burst cycle, with key points marked by colored symbols that appear in all of the plots. Starting from the yellow star when Ca_i is at its minimum, the trajectory moves on the superslow timescale associated with h along the stable lower branch of S to the increasing h direction until it reaches the lower fold (SN) at the green circle. We must also consider the dynamics of the calcium subsystem during this slow drift. In that subsystem, Ca_i is the slow variable, but the projection of the trajectory to (Ca_i, Ca_{tot}, l) lies on the Ca_i-nullsurface [Fig. 3(b)]. This nullsurface does depend on V, but there is little change in V since V remains hyperpolarized and is slaved to h, and hence there is little change in Ca_i.

The situation changes when the trajectory reaches the fold of S, where the fast (V, n) dynamics causes the trajectory to jump up to the stable periodic orbit branch, after which it exhibits voltage spikes and drifts to the left under the h dynamics since the trajectory stays above the h-nullcline [Fig. 3(c)]. Such spiking (black) continues for some time until the trajectory is attracted to a stable segment of the upper branch of S, causing a switch from voltage spikes to a voltage DB (red).

We claim that the transition from spiking to DB is induced by the jump up of Ca_i. To understand this, we consider the effect of Ca_i

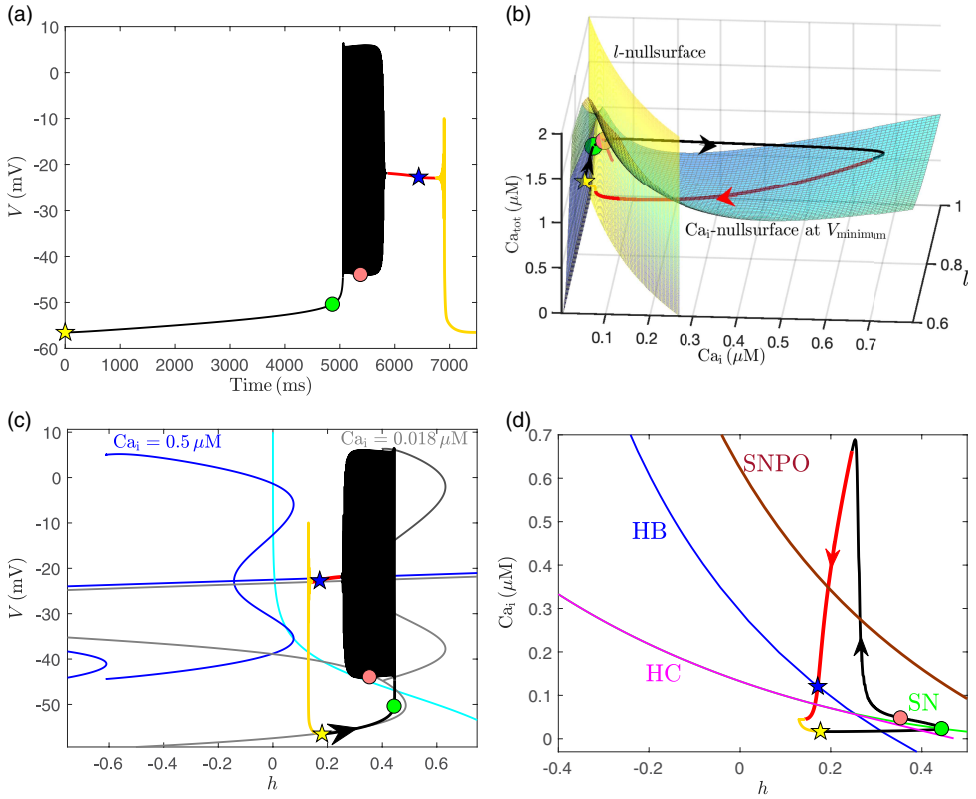

FIG. 3. Simulation of one cycle of the DB bursting solution generated by (1), together with the basic structures of voltage and calcium subsystems, for $g_{CAN} = g_{NaP} = 2.5$ nS and other parameters at default values. The yellow star denotes the starting point of the solution cycle shown. The green dot and the blue star indicate where the trajectory intersects the SN bifurcation and the HB bifurcation in the (h, Ca_i)-space, as shown in (d). The pink dot indicates where the trajectory intersects the *transition curve* [the pink curve near the l-nullsurface in (b)]. (a) Temporal evolution of V. (b) Nullsurfaces of Ca_i (blue) and l (yellow) for the calcium component with V at its minimum in the (Ca_i, Ca_{tot}, l)-space. The increase of V will move the Ca_i-nullsurface to the lower right but will not affect the l-nullsurface. The colorful curve denotes the trajectory from (a). When the transition curve is reached at the pink dot, the trajectory intersects the saddle-node curve of the Ca_i nullsurface [in the full (V, Ca_i, Ca_{tot}, l)-space]. (c) The trajectory from (a) and the effect of Ca_i on the bifurcation diagram for the (V, n) system, projected onto the (h, V)-space, along with the h-nullcline (cyan). Increasing Ca_i results in a shift of the bifurcation diagram to the upper left (gray to blue) and changes the fixed point in the upper branch of S from unstable to stable as Ca_i increases above 0.2856 μM. (d) The curves of the homoclinic bifurcation (HC, magenta), saddle-node (SN) bifurcations corresponding to the lower fold of S (green), the Hopf bifurcation curve (HB, blue), the SNPO bifurcation curve (brown), and the trajectory in the (h, Ca_i) space.

on the voltage subsystem. We return to the 2-parameter bifurcation diagram in the (h, Ca_i)-space generated by treating Ca_i as the second bifurcation parameter for (V, n) and following in (h, Ca_i) the critical bifurcation points including HC, SN, HB, and SNPO from the 1-parameter bifurcation diagram [see Fig. 3(d)]. In the (h, Ca_i)-space, the trajectory moves rightward from the yellow star and starts oscillating as it passes the SN curve at the green dot. When Ca_i jumps up (the cause of which we consider below), the trajectory in (h, Ca_i) crosses the SNPO curve and reaches its maximum Ca_i value. As a result, the trajectory lies on the right side of the SNPO when viewed in the (h, V)-space [see Fig. 3(c)] and, therefore, spirals into the attracting part of the upper branch of S and transitions to the DB phase. During this DB, a slow decrease of Ca_i occurs as the trajectory in the (Ca_i, Ca_{tot}, l)-space evolves along the right branch of the Ca_i-nullsurface [see Fig. 3(b)]. This slow drift will bring the trajectory in the (h, Ca_i)-space back across the HB curve at the blue star in Fig. 3(d). This crossing results from a rightward shift of the fast subsystem structures in the bifurcation diagram in the (h, V)-space [see Fig. 3(c)] such that the trajectory that travels to the left crosses the HB bifurcation at the blue star and reaches the unstable portion of the upper branch of equilibria on S. As a result, the trajectory spirals away from this branch and jumps back to the lower branch of S, where it returns to the yellow star. It follows that the timing of the exit from the DB phase should correspond to a way-in/way-out phenomenon,[6,7,18,19] rather than being immediate upon a crossing of the HC bifurcation curve.

Finally, we investigate how the jump up of Ca_i occurs. To do so, we compute a bifurcation curve corresponding to the fold of the equilibrium solution of the Ca_i equation by treating V and (Ca_{tot}, l) as fixed parameters. Specifically, we vary the latter two simultaneously along a one-dimensional curve (the solution curve of the full system) in a two-dimensional space. When the trajectory projected

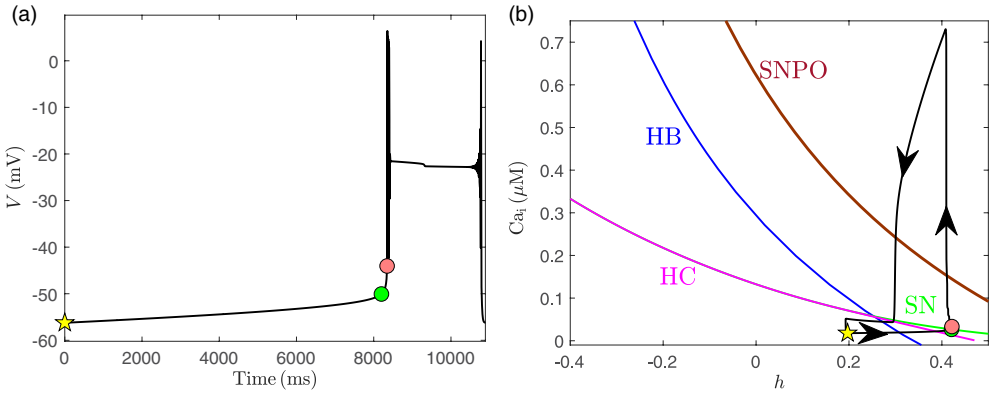

FIG. 4. Parameters are as in Fig. 3 except Ca_i is ten times faster, and h, Ca_{tot}, l are half as fast as before. (a) Temporal evolution of V. (b) Projection of the bursting solution from the left panel onto the 2-parameter bifurcation diagram in the (h, Ca_i)-space. Symbols all have the same meaning as in Fig. 3. The delay in time between the jump up of Ca_i and the jump up of V and the delay between the jump up of Ca_i and the beginning of DB are both shorter than the delays in Fig. 3.

to the (Ca_i, Ca_{tot}, l)-space crosses this transition curve [Fig. 3(b), pink curve] at the pink dot, the trajectory reaches the fold of the Ca_i-nullsurface, which will initiate a slow jump of the trajectory to larger Ca_i if the timescale separation between Ca_i and Ca_{tot}, l is big enough. However, note that Ca_i is ten times slower than V (see Table III). As a result, multiple additional voltage spikes occur after the crossing of the pink dot before the Ca_i value becomes large enough to initiate the DB.

1. Timescale analysis

Past work[1,30] has shown that DB bursting can be produced by two timescale dynamical systems. To identify how many timescales are needed for DB bursting in model (1), we speed up Ca_i so that V, n, Ca_i evolve on the fast timescale. As a result, model (1) reduces to a two timescale system. Figure 4 shows that exaggerating the timescale separation between the new fast classes (V, n, Ca_i) and the superslow classes (h, Ca_{tot}, l) still preserves the DB bursting dynamics. This suggests that DB bursting in this paper is also a two timescale phenomenon. Since Ca_i is now evolving on a fast timescale, the time difference between the green dot and the pink dot and the number of spikes before the depolarization block phase are significantly reduced.

Note that there is a small gap between the SN and HC curves in the (h, Ca_i)-space [see Fig. 3(d)]. As discussed in Refs. 42 and 43 and illustrated in Fig. 5, if Ca_{tot} and l are made slower than h, then the trajectory in (h, Ca_i) is able to cross the gap multiple times, with each crossing taking long enough to allow for a brief N (square-wave) burst so that there are multiple N bursts before the DB burst. This adjustment hence leads to the transition from the regime of DB bursting solutions, with one episode of rapid V spikes between each depolarization block event, to the regime of N/DB bursting solutions, which feature multiple full N bursts between DB bursts. Although the example in Fig. 5 is exaggerated, this type of pattern is seen experimentally.[4] Later, we will discuss another mechanism that can produce related mixtures of N and DB bursting when g_{NaP} is increased.

C. Bifurcation analysis for the mixed bursting (MB) solution

In this section, we consider the mixed bursting dynamics [Fig. 6(a)] produced by (1) for $g_{CAN} = 1$ nS, $g_{NaP} = 2.5$ nS with all the other parameters at their default values (Table I). While the model can generate a variety of mixed bursting solutions across different parameter sets, for the case that we consider, one cycle of the mixed bursting solution consists of one I_{NaP}-dependent (N) burst (shown in red), one depolarization block (DB) burst (shown in yellow), and one $I_{NaP} + I_{CAN}$-dependent (N + C) burst (shown in black). That is, we consider a mixed bursting pattern that is at the core of the model dynamic repertoire, in that it features regular alternations of the three primary model behaviors. The mechanisms underlying the pure N bursting and pure DB bursting solutions have been explained in detail in Secs. IV A and IV B. The N + C bursting solution depending on both I_{NaP} and I_{CAN} has been well studied across multiple past works.[22,39,42,43] In order to understand how the mixed bursting solution arises in (1), we, therefore, only need to understand how the transitions between the three different bursts within each mixed bursting cycle occur. We note that similar mixed bursting solution patterns have also been observed and studied in other respiratory neuron models. By applying bifurcation analysis and fast–slow decomposition, Refs. 42 and 43 explained the mechanisms underlying a mixed N/N + C bursting solution that consists of N + C bursts separated by sequences of N bursts. It was shown that the transition from the N burst to the N + C burst in the mixed N/N + C bursting solution is associated with the calcium dynamics.

In the following, we uncover the mechanisms underlying the mixed bursting solution produced by (1) [see Fig. 6(a)] in two steps: First, we demonstrate directly that the transitions between N, DB, and N + C bursting solutions in the mixed bursting solution are also related to the calcium dynamics. Specifically, the N burst (red burst) results because it has the slowest evolution of Ca_i relative to h; faster changes in Ca_i relative to h lead to the transition from the N burst to the DB burst (yellow burst), whereas a moderate rate of change of Ca_i relative to h after the DB bursting solution

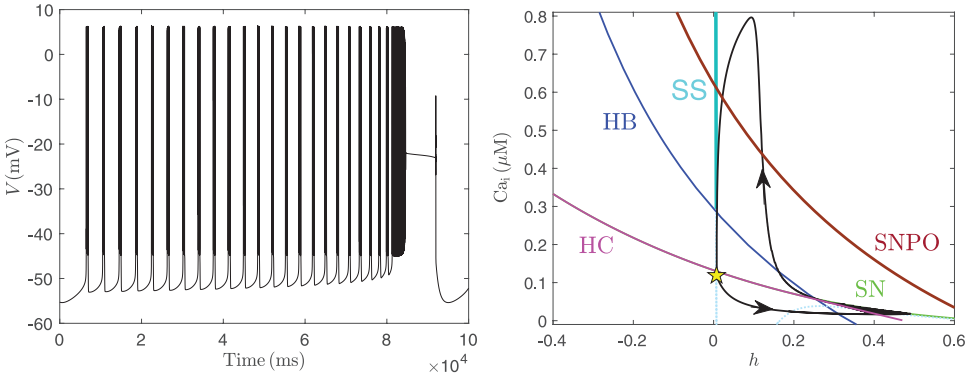

FIG. 5. Simulation of one cycle of the N/DB bursting solution, produced by (1) for the same parameter values as in Fig. 3 except we make Ca_{tot} and I ten times slower than h. Left: Temporal evolution of V. Right: Projection of the N/DB bursting solution onto the 2-parameter bifurcation diagram in the (h, Ca_i)-space, the same as shown in Fig. 3(d). The cyan curve denotes the fixed points of the (V, n, h) subsystem with stable (unstable) branches drawn as solid/thick (dashed/thin) curves.

results in the transition to the N + C bursting solution (black burst). Second, we explain the factors that result in these modulations of the relative rate of change of Ca_i across the course of the burst cycle.

1. Different evolving rates of Ca_i relative to h lead to different types of bursts in the mixed bursting solution

Among the three bursts of the mixed bursting solution shown in Fig. 6(a), the red burst has the slowest movement of Ca_i relative to h. As a result, the red trajectory projected to the (h, Ca_i) parameter space can cross the SN and HC bifurcation curves to form an N burst without any jump up in Ca_i [see Fig. 6(b)]. In contrast, the trajectories of the subsequent two bursts in the (h, Ca_i)-space [Fig. 6(b), yellow/cyan and black curves] jump to larger Ca_i values before traversing from the SN to the HC curve because they have faster changes in Ca_i relative to h compared with the N bursting case. Hence, both bursts occur along with a jump up of Ca_i, resulting in either DB or N + C solutions. Figure 6(b) shows that both the yellow and black trajectories cross the SNPO bifurcation curve in the (h, Ca_i)-space. As discussed in the pure DB burst case, such a crossing naturally leads to DB bursting solutions (e.g., the yellow DB burst solution) because after it occurs, the only fast subsystem

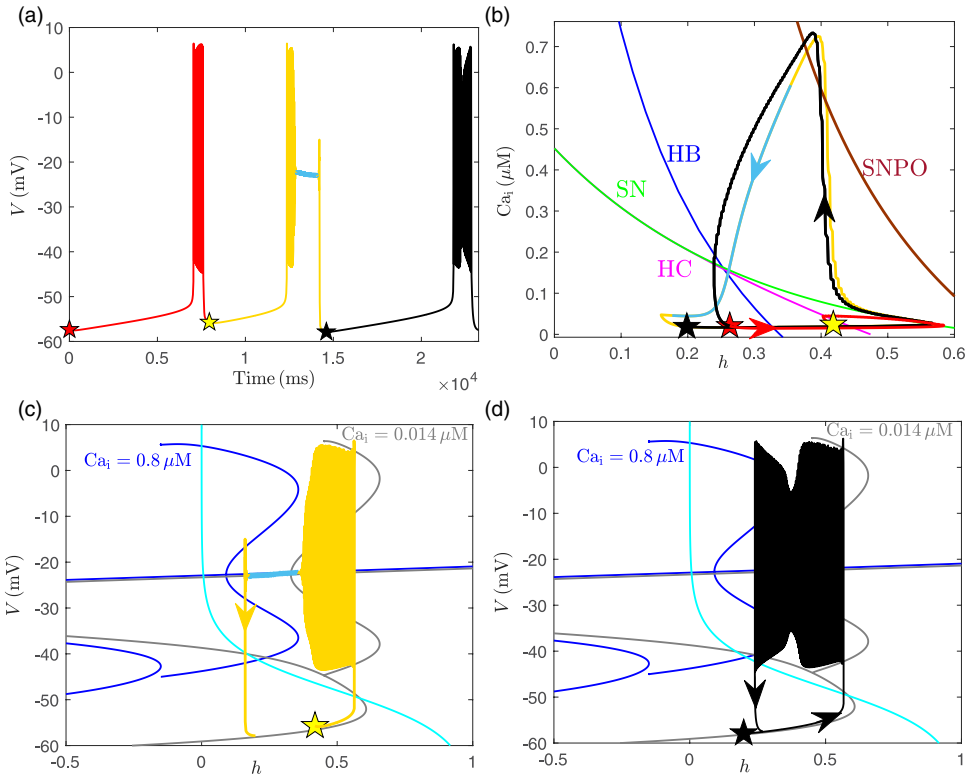

FIG. 6. Simulation of one cycle of the mixed bursting solution generated by (1), together with the basic structures of subsystems (V, n, h), for $g_{CAN} = 1$ nS, $g_{NaP} = 2.5$ nS, and other parameters as default. (a) Temporal evolution of V. (b) Projection of the trajectory from (a) and 2-parameter bifurcation curves of HC, SN, HB, and SNPO onto the (h, Ca_i)-space. (c) The DB burst solution trajectory (yellow) and the effect of Ca_i on the bifurcation diagram for the (V, n) system, projected onto the (h, V)-space. (d) The N + C burst solution trajectory (black) and the effect of Ca_i on the bifurcation diagram for the (V, n) system, projected onto the (h, V)-space. Color coding and symbols have the same meaning as in Fig. 3.

attractor is the equilibrium state at elevated voltage. However, the crossing between the black trajectory and the SNPO curve gives a N + C burst rather than a DB burst. To understand the difference between the two crossings, we make use of the 1-parameter bifurcation diagram of the (V, n) fast subsystem with h treated as a parameter [see Figs. 6(c) and 6(d)]: the gray (respectively blue) curve denotes the bifurcation diagram of the voltage subsystem that is obtained for Ca_i at 0.014 μM (respectively 0.8 μM). We can see that as Ca_i increases, the bifurcation diagram will shift to the left.

Since the yellow burst has the fastest changes in Ca_i relative to h among the three bursts, the moving periodic orbit family, as it evolves from the gray position to the blue due to the increase of Ca_i, completely overtakes the yellow trajectory [see Fig. 6(c)]. After that, the trajectory jumps down to the attracting part of the upper branch of S (blue) to form a DB, as shown in dark cyan. As explained in the pure DB bursting case in Sec. IV B, the DB will then be terminated after passage through the HB bifurcation as Ca_i decreases again. On the other hand, the black burst is accompanied by a moderate rate of change of Ca_i relative to h so that although the trajectory still crosses the SNPO bifurcation as in the yellow burst, it is not fully overtaken by the leftward moving periodic orbit to form a DB [see Fig. 6(d)]. Instead, the black burst trajectory in the (h, V)-space tracks along with the leftward moving periodic orbit family during the increase of Ca_i, resulting in a decrease in the spike amplitude, and then tracks along with the rightward moving periodic orbit as Ca_i later decreases, resulting in a ramping up of spike amplitude. As the trajectory eventually passes the HC bifurcation curve, it jumps back to the lower branch of S.

2. Why Ca_i changes at a different rate relative to h at the start of the different burst types

It remains to explain why Ca_i evolves at different rates at the onsets of the three bursts. To this end, we plot the projection of the mixed bursting solution onto the (Ca_i, Ca_{tot}, l)-space and the (Ca_{tot}, l)-space in Fig. 7. From Fig. 7(b), we can see that Ca_{tot} and l are smallest at the beginning of the N burst (red star), largest at the beginning of the DB burst (yellow star), and moderate at the beginning of the N + C burst (black star). In the following, we use Fig. 7(a) to understand the changes of Ca_{tot} and l values across the burst cycle. We end the section by showing that these changes are the key factors that lead to different relative evolving rates of Ca_i in different bursts.

Before explaining the changes of Ca_{tot} and l values across the burst cycle, we need to have a better understanding of the way-in/way-out effect in the DB burst as the voltage is pinned along the upper branch of S [see Fig. 6(c), dark cyan curve]. In Fig. 7(a), as the trajectory of the yellow burst reaches the fold of the Ca_i-nullsurface, the trajectory jumps to the right branch of the Ca_i-nullsurface [this is difficult to see in Fig. 7(a) due to the overlap of the yellow and black curves, but it can be seen as the switch in (Ca_{tot}, l) from increasing to decreasing in Fig. 7(b)]. After the jump, the DB trajectory (cyan) travels along the right branch of the V-dependent family of Ca_i-nullsurfaces until passing the curve of lower folds and jumping back to the left branch. This jump will bring the trajectory across the HB bifurcation of the (V, n) subsystem [see Fig. 6(c)]. Due to a way-in/way-out phenomenon as mentioned in Sec. IV B, after the crossing, there is a delay before V jumps down to the lower branch of the equilibria S to end the DB. Hence, in Fig. 7(a), because V is pinned along the upper branch of the equilibria S after the jumping down of Ca_i, the cyan trajectory reaches and travels along the left branch of a Ca_i nullsurface that corresponds to V much larger than −60 mV and thus lies to the right of the one plotted in Fig. 7(a). That is, both V and Ca_i after the jumping down of Ca_i in the DB solution are larger than at the red star (the landing point of the black trajectory at the left branch of the Ca_i nullsurface at $V = -60$ mV). Moreover, the extended delay time in the DB burst allows the cyan trajectory to travel in the increasing Ca_{tot} and l direction before switching to the subsequent N + C burst at the black star.

We now explain why the Ca_{tot} and l values at the red star are smaller than that at the black star, which are smaller than those at the yellow star [see Fig. 7(b)]. As discussed above, while the DB burst (yellow + cyan) and N + C burst (black) trajectories jump down to the left branch of Ca_i-nullsurfaces at similar values of Ca_{tot} and l [see Fig. 7(a)], Ca_{tot} and l are able to increase after they reach the minimum in the DB burst solution until the trajectory jumps to the black star. This leads to larger Ca_{tot} and l values at the black star than at the red star. Next, we explain why Ca_{tot} and l values at the black star are smaller than that at the yellow star. This is related to the different evolution rates of Ca_{tot} and l as well as the associated duration of time over which they evolve. Since V evolves along the upper branch of S during the DB, I_{Ca} in $J_{PM_{in}}$ stays on [see Eq. (1)] and hence will speed up the increase of Ca_{tot} in the cyan trajectory. Now, Ca_i is also larger during the DB than during the N burst, but this is a minor difference and it tends to slow down the growth not only of Ca_{tot} but also of l. Thus, the net effect of the DB is that, as shown in Fig. 7(b), the cyan trajectory near the red star moves to the increasing Ca_{tot} direction at a faster rate, whereas the increase of l is slower than at the red trajectory. Note that the extended delay time in the DB burst solution (due to the way-in/way-out effect) during which the cyan trajectory moves to the right in the (Ca_{tot}, l)-space is shorter than the duration of the full red trajectory (i.e., the entire N burst). That is, after reaching the minimum of Ca_{tot} and l values, there is more time for the red trajectory to travel in the increasing Ca_{tot} and l directions than the cyan trajectory. As a result, we obtain a slightly larger Ca_{tot} value and a much larger l value at the yellow star than at the black star. These considerations, therefore, explain the variations of Ca_{tot} and l values across different bursts.

Note that the larger the Ca_{tot} and l are, the faster the Ca_i evolves. Ca_i, therefore, evolves slowest at the red star, fastest at the yellow star, and moderately at the black star. On the other hand, while the h values at the black and red stars are similar, they are both smaller than the h value at the yellow star [see Fig. 6(b)]. Hence, h at the yellow star evolves slower than at the other two stars. Therefore, the evolving rate of Ca_i relative to h is slowest at the red star, fastest at the yellow star, and moderate at the black star, as claimed.

V. TRANSITIONS BETWEEN DIFFERENT ACTIVITY PATTERNS

We have used bifurcation analysis to study how I_{NaP} and I_{CAN} interact within a single model pre-BötC neuron to generate various activity patterns such as plateau bursting, including N, C, and N + C

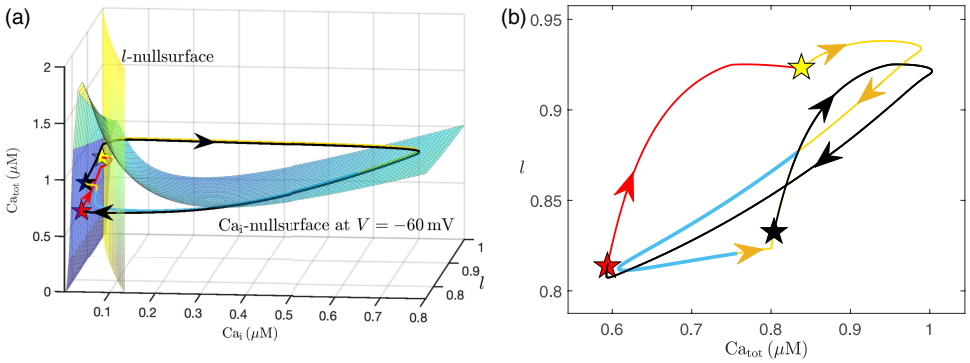

FIG. 7. $g_{CAN} = 1$ nS, $g_{NaP} = 2.5$ nS. (a) Nullsurfaces for Ca_i and l for the calcium component with $V = -60$ mV. The colorful curve denotes the trajectory from Fig. 6(a). (b) Projection of the solution from Fig. 6(a) onto the (Ca_{tot}, l)-space. Color codings and symbols are the same as in Fig. 6.

bursting patterns, DB bursting, and mixed bursting. In this section, we consider how the transitions between these different bursting patterns occur as the values of the parameters g_{NaP} and g_{CAN} are varied. Recall that model activity patterns over the two-parameter (g_{NaP}, g_{CAN}) space are summarized in Fig. 1(a).

A. From N/N + C-bursting to N/DB bursting to pure DB bursting with high g_{NaP}

We fix g_{NaP} at a high value and consider how activity patterns change as g_{CAN} varies. As an example, we set $g_{NaP} = 4$ nS. Figure 1(a) shows that the increase of g_{CAN} leads to a transition from N/N + C to N/DB to pure DB bursting dynamics. Time series of the three solutions are shown in the left panel of Fig. 8. The right panel shows the corresponding bifurcation diagrams in the (h, Ca_i) parameter space, together with the projections of the trajectories. Increasing g_{CAN} causes two qualitative changes in the solution patterns: (1) The N + C burst at the end of the N/N + C bursting solution will be replaced by a DB burst. (2) The number of N bursts will eventually decrease to 0, resulting in a DB on every burst and hence a loss of mixed bursting. Below, we use the bifurcation diagrams shown in Figs. 8(b), 8(d), and 8(f) to explain how the two changes occur. We have already seen in the analysis of the DB burst solution that a DB can occur when Ca_i shifts the voltage subsystem bifurcation structure sufficiently that the trajectory crosses the SNPO curve. As g_{CAN} increases, less of an increase in Ca_i is needed to achieve this crossing because g_{CAN} multiplies the increasing function $CAN_\infty(Ca_i)$ in Eq. (2). Indeed, in Figs. 8(b), 8(d), and 8(f), we see that as g_{CAN} increases, the projection of the SNPO curve to the (h, Ca_i) plane shifts to lower Ca_i levels. As a result, when g_{CAN} is switched from 0.5 nS to 2 nS or 4 nS, the trajectory can cross the SNPO curve, resulting in DB bursting events [e.g., see Figs. 8(c) and 8(e)].

To see why N bursts disappear as g_{CAN} increases, we note that each N burst is initiated (respectively terminated) by the curve of SN (respectively HC) bifurcations [see Fig. 8(b)]. The two curves eventually meet, corresponding to a curve of SNIC bifurcations.[9,34] If Ca_i jumps up before the trajectory reaches the HC or SNIC bifurcation during the active phase, then a DB will occur instead of an N burst. As g_{CAN} increases, the projections of the HC and SNIC curves shift to lower Ca_i levels. Moreover, the trajectory during the active phase moves to the left at a slower rate since bursting initiates at smaller h values. Hence, it takes more time for the trajectory to reach the HC and SNIC curves. That is, a transition to a DB becomes more likely as g_{CAN} becomes larger. As a result, when g_{CAN} is switched from 0.5 nS to 2 nS, the trajectory can get above the HC and SNIC curves on every second burst, resulting in a single N burst per cycle. A further increase of g_{CAN} to 4 nS allows the trajectory to cross the SNPO curve on every burst, and hence, a pure DB bursting solution results (see Fig. 8).

The two effects of increasing g_{CAN} on model activity patterns can also be used to understand how the transitions between different bursting patterns occur for other g_{NaP} values in Fig. 1(a): as g_{CAN} increases, plateau bursts (including N, C, and N + C bursts) will eventually be replaced by the pure DB burst. For g_{NaP} values that lie in the mixed bursting range [Fig. 1(a), green region], the increase of g_{CAN} will induce more complicated transitions. For example, a transition from N/N + C to mixed bursting (N/DB/N + C) to N/DB to DB bursting can occur for $g_{NaP} = 3$ nS. In this case, in contrast to the situation when $g_{NaP} = 4$ nS, before the N + C burst is replaced by the DB burst, they coexist, along with the N burst, for a small range of g_{CAN}, where mixed bursting solutions occur.

In summary, the increase of g_{CAN} will switch the model behavior from plateau bursts to DB bursts by altering the position of the HC, SNIC, and SNPO curves in the (h, Ca_i) plane. Depending on the g_{NaP} value, this transition can occur directly or indirectly through mixed plateau/DB dynamics.

B. From pure DB bursting to N/DB bursting with intermediate g_{CAN}

In this section, we consider various fixed values of g_{CAN} and explore the effect of g_{NaP} on activity patterns. As discussed in Sec. V A, for g_{CAN} sufficiently large, only DB bursts occur, and hence, variation of g_{NaP} within the range (0, 5) will not introduce any transition of activity patterns [see Fig. 1(a)]. We hence explore transitions that occur for g_{CAN} smaller than 3.5 nS. For example, when $g_{CAN} =$ 2 nS, the increase of g_{NaP} leads to the transition from a pure DB burst to a N/DB burst, as shown in Fig. 9. The pink dots in Fig. 9 have the same meaning as in Fig. 3: these indicate where the jump up of Ca_i occurs. The solid (respectively dotted) cyan curves in the panels in the right column denote the stable (respectively unstable) equilibria of the (V, n, h) subsystem.

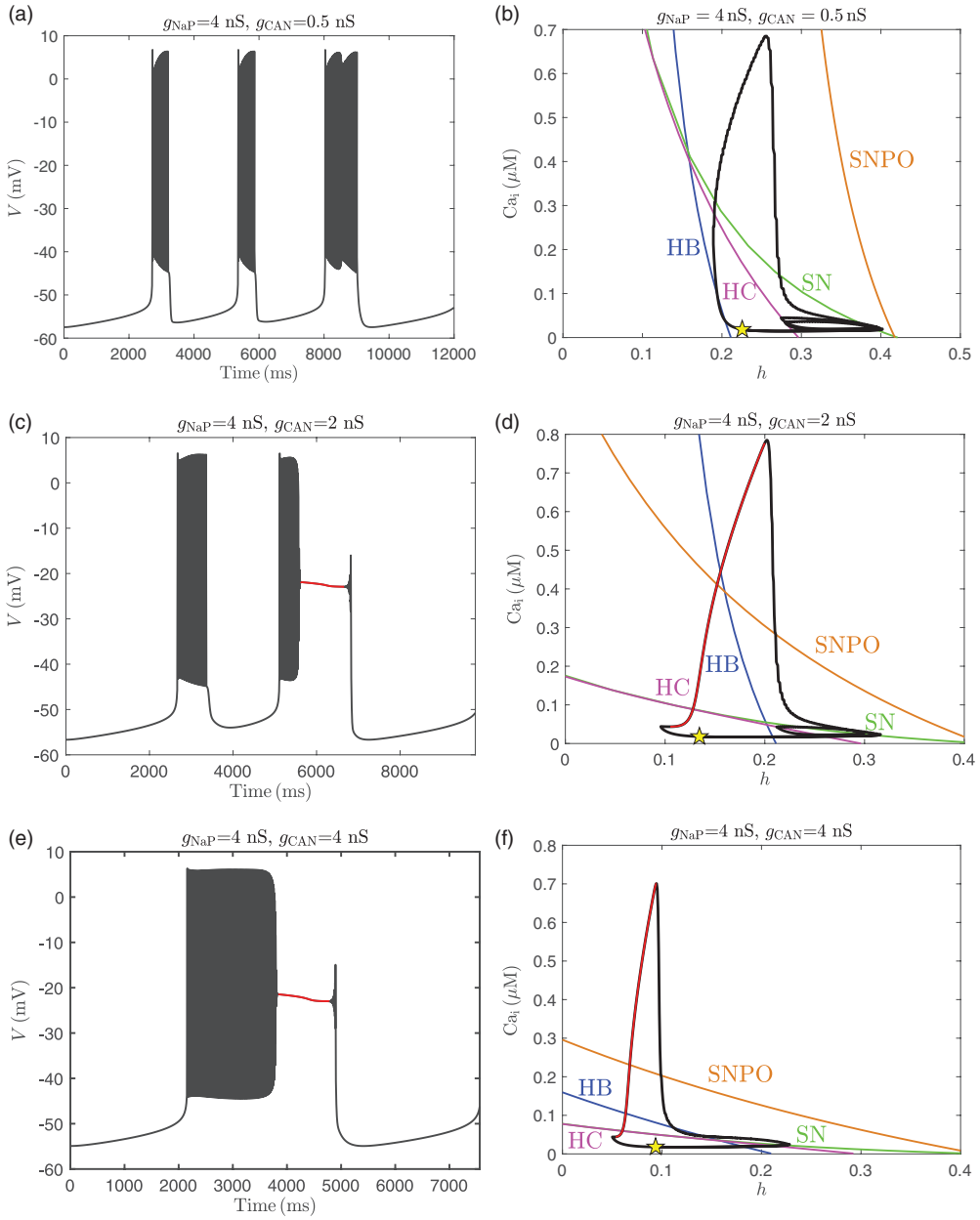

FIG. 8. Simulation of one cycle of bursting solution, produced by (1) with parameters $g_{NaP} = 4$ nS and (a) and (b) $g_{CAN} = 0.5$ nS, (c) and (d) $g_{CAN} = 2$ nS, and (e) and (f) $g_{CAN} = 4$ nS. Left: Temporal evolution of V. Right: Projection of the solution (black) from the left onto the (h, Ca$_i$)-space, together with bifurcation curves of HC, SN, HB, and SNPO. Color codings and symbols have the same meaning as in Fig. 3.

When g_{NaP} is low, the (V, n, h) subsystem has a stable equilibrium point for each sufficiently small value of Ca$_i$ [Fig. 9(b), solid cyan curve]. Starting from the yellow star, the trajectory travels rightward to the stable SS curve until Ca$_i$ jumps up to a larger value at the pink dot. This jump brings the trajectory across the SNPO curve, resulting in a DB as discussed before. Hence, the model exhibits pure DB bursting solutions for low g_{NaP} values. In contrast to the DB bursting solution in Sec. IV B, where the jump up of Ca$_i$ follows the elevation of voltage, here jumping up of Ca$_i$ occurs first, leading to a voltage increase.

For large g_{NaP} values, the (V, n, h) subsystem lacks a stable equilibrium point and exhibits bursting dynamics when Ca$_i$ is small

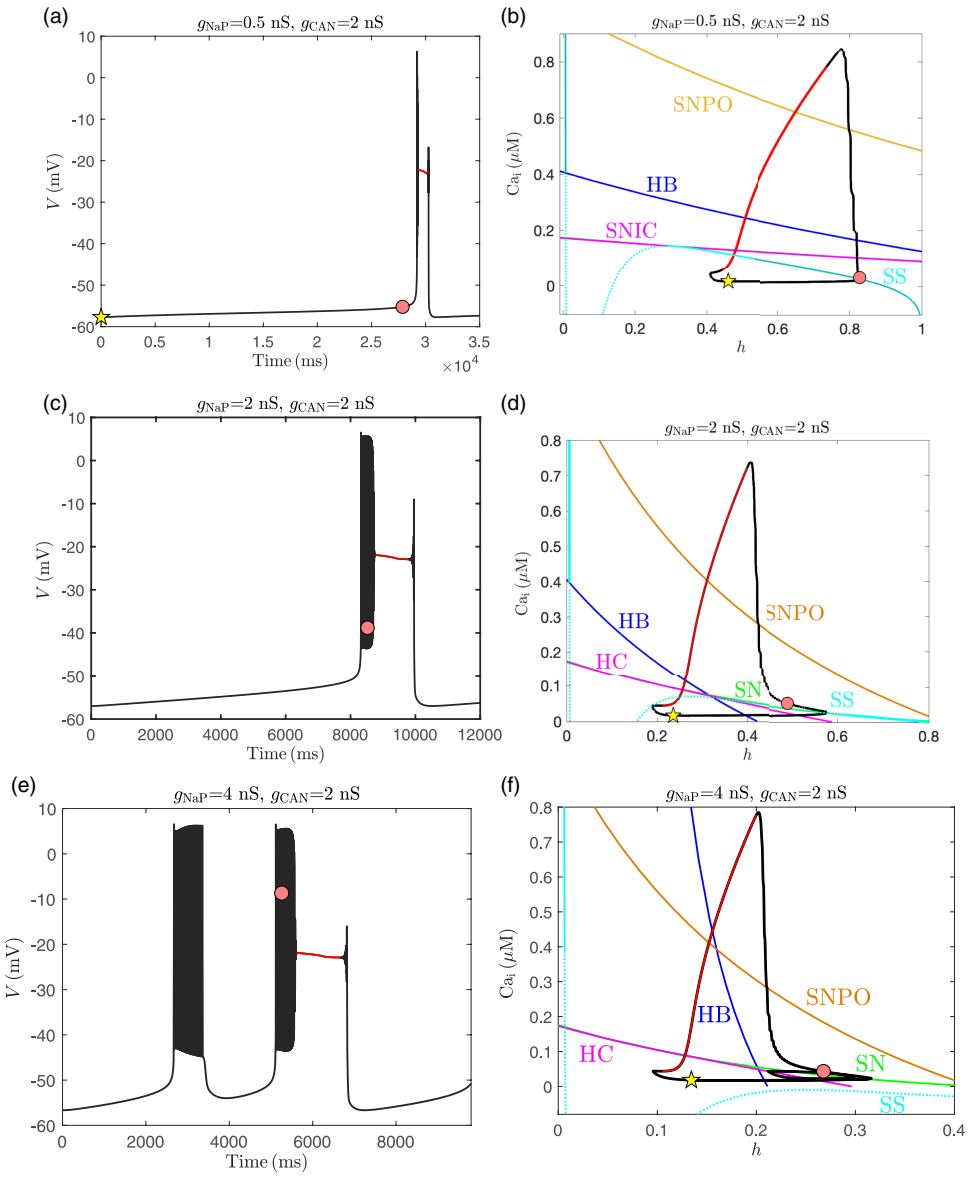

FIG. 9. Simulation of one cycle of bursting solution, produced by (1) with parameters $g_{CAN} = 2$ nS and (a) and (b) $g_{NaP} = 0.5$ nS, (c) and (d) $g_{NaP} = 2$ nS, and (e) and (f) $g_{NaP} = 4$ nS [same as Figs. 8(c) and 8(d)]. Left: Temporal evolution of V. Right: Projection of the solution (black) from the left onto the (h, Ca_i)-space, together with bifurcation curves of HC, SN, HB, and SNPO and the fixed points SS of the (V, n, h) system (cyan; solid where attracting, dashed otherwise). Color codings and symbols have the same meaning as in Fig. 3.

[see Figs. 9(e) and 9(f)]. As a result, one or more N bursts can occur before the jump up of Ca_i yields a depolarization block. Hence, the N/DB bursting solution results.

For intermediate g_{NaP} values [e.g., $g_{NaP} = 2$ nS in Figs. 9(c) and 9(d)], the fixed point of the (V, n, h) voltage system switches its stability during the silent phase of calcium. Specifically, starting with low calcium, the voltage system is in a quiescent mode, with low voltage, while the trajectory advances in the direction of increasing h. After the trajectory crosses the SN curve, the system switches to a potential N burst. In this intermediate case, however, before the trajectory can cross the HC curve and terminate the burst, it jumps up to the elevated branch of Ca_i values [Fig. 9(d)]. Hence a pure DB bursting solution results.

One natural question to ask is why the trajectory in the case of $g_{NaP} = 4$ nS is able to cross the gap between the SN and HC curves to form an N burst, whereas the trajectory when $g_{NaP} = 2$ nS fails to do so before Ca_i jumps up. To answer the question, we note that with increased g_{NaP}, lower h and Ca_i are needed to initiate the burst at the SN curve. Notice that the lower level of h corresponds to a faster increasing rate of h and hence it takes less time for the trajectory to reach the SN curve. As a result, less Ca_{tot} and l can be built up before bursting occurs at the SN bifurcation. This leads to a slower rate of change of Ca_i, as discussed in Sec. IV C. That is, as g_{NaP} increases, Ca_i increases slower at the SN curve, and hence, N bursts become more likely to occur. Note that as g_{NaP} increases, h also decreases slower after the trajectory crosses the SN curve, as discussed in Sec. V A.

However, the slower increase of Ca_i dominates and allows the trajectory to cross the HC curve before it can jump up to the SNPO curve in the case when $g_{NaP} = 4$ nS.

To summarize, for $g_{CAN} = 2$ nS, the N burst will arise as g_{NaP} becomes large enough. Moreover, in contrast to the sensitivity of the DB to variations of g_{CAN}, the maintained depolarization in the solution persists as g_{NaP} increases from 0.5 nS to 4 nS. This is because while the SNPO curve shifts to lower h levels as g_{NaP} increases, the trajectory makes the same shift and hence is still able to cross the SNPO curve as Ca_i jumps. Hence, I_{NaP} is less important for the DB burst than I_{CAN}, as observed experimentally.[4]

Alternatively, when g_{CAN} is smaller but not too small (e.g., $g_{CAN} = 1.0$ nS), the model can produce a C burst at a small g_{NaP} value rather than a DB burst because even a jump in Ca_i is not strong enough to bring the trajectory across the SNPO curve. Starting from the C bursting regime (e.g., $g_{NaP} = 0.5$ nS, $g_{CAN} = 1$ nS), an increase of g_{NaP} that shifts the SNPO curve to lower Ca_i levels can make the crossing happen; that is, a transition from a C burst to a DB burst can occur as g_{NaP} increases (e.g., at $g_{NaP} = 1.8$ nS, $g_{CAN} = 1$ nS). A further increase of g_{NaP} can lead to N/DB bursting, as discussed before. Finally, for parameter values in the mixed bursting (N/DB/N + C) regime [Fig. 1(a), green region], a crossing of the SNPO curve does not necessarily lead to a DB; an N + C bursting solution can occur, as seen in Sec. IV C. Hence, as the increase of g_{NaP} takes the parameters across the mixed bursting region in the parameter space, some complicated transitions can arise. For example, the transition from a DB burst to a mixed burst (N/DB/N + C) to an N/DB burst as well as the transition from a DB burst to an N + C burst to a mixed burst to an N/N + C burst to an N/DB burst can happen. When g_{CAN} is small enough so that there is no DB, a transition from (silence to) an N + C to N/N + C burst occurs because the increase of g_{NaP} enables N bursts to occur.

VI. DISCUSSION

In this work, we consider a model for burst-capable respiratory neurons in the pre-BötC. The model that we study was proposed by previous authors to encompass both prenatal and postnatal pre-BötC neural dynamics and represents a suitable setting in which to investigate changes in the pre-BötC activity across embryonic development.[4] The key results of this paper are explanations of the dynamic mechanisms underlying multiple forms of bursting that the model can exhibit individually or in combinations, including the mapping from persistent sodium and CAN current conductances to emergent burst patterns. This work establishes that a balance in these conductances supports complicated mixed bursting solutions that feature repeated cycling through multiple types of bursts, while imbalances that favor persistent sodium or CAN currents promote square-wave bursts or bursts featuring intervals of depolarization blocks, respectively. These results suggest that a developmental increase in the persistent sodium conductance would not in itself be enough to eliminate DB bursts; a reduction of the CAN conductance appears to be essential, and the combination of these changes at the individual cell level is predicted to be sufficient to shift the pre-BötC neuron activity from the patterns observed embryonically to those seen after birth.

After nondimensionalizing the model to expose the timescales on which its components evolve, we used the methods of fast–slow decomposition and bifurcation analysis to analyze the mechanisms underlying various patterns of model dynamics. The model produces three main types of bursting, I_{NaP}-dependent (N), $I_{NaP} + I_{CAN}$-dependent (N + C), and depolarization block (DB) bursting, the first of which is a form of square-wave bursting.[28] Mixed bursting (MB) solutions featuring combinations of all three burst types can occur in certain parameter regimes, and the MB state acts as an organizing center for model dynamics: starting from MB activity, variations of specific parameters favor corresponding burst types over others, and from our analysis of the mechanisms promoting each form of bursting within the MB regime, we can understand these parameter-dependent effects. Specifically, we showed that in solutions with repeating burst cycles, the type of burst that emerges on a particular cycle is determined by the levels of two slowly evolving quantities, the combined intracellular and ER calcium concentration (Ca_{tot}) and the fraction of non-inactivated IP_3 channels (l; Fig. 7), at the start of the cycle, and we explained the mapping from these variables to the emergent burst types. Once we established that relationship, we could explain why the CAN current promotes DB bursting, via its effects on the locations of the HB and SNPO bifurcation curves of the fast subsystem (Fig. 8), consistent with previous results on CAN-based bursting.[30] Similarly, we could explain why the NaP current promotes square-wave N bursting, via its effects on the SN and SNIC or HC bifurcation curves of the fast subsystem (Fig. 9); the onset of bursting for larger persistent sodium conductances occurred at lower levels of the persistent sodium current inactivation variable h as well as with smaller values of all of the calcium-related variables (Ca_i, Ca_{tot}, l), allowing for the completion of a burst without a jump up of the intracellular calcium concentration (Ca_i).

Past computational work on the dynamics of individual pre-BötC neurons has included two streams. One has focused on the development of models that take into account successively more biological detail. After initial models focused on single burst mechanisms,[3,30,33] subsequent models either combined mechanisms based on persistent sodium and calcium dynamics, presenting more complete representations,[8,11,39] or honed in on specific issues such as sigh generation[40] or effects of extracellular potassium concentration.[1] Another path of study emphasizes the mathematical mechanisms underlying model dynamics, although Refs. 1, 8, and 30 include such considerations as well. While the original model of bursting based on the persistent sodium current[3] exhibits standard square-wave bursting with a single slow variable—and indeed represents a prime example of this form of dynamics—subsequent models have involved two slow variables[30] or else several slow variables and a third timescale. Past mathematical analysis has taken on these issues[8,22] and, in some cases, has elucidated which forms of pre-BötC dynamics, in which models, require three timescales.[42,43] The current paper advances this research direction by (1) analyzing MB patterns that combine three burst types and serve as an organizing center for many of the bursting patterns observed across the previous models and (2) providing the first analysis of depolarization block (DB) bursting in a pre-BötC neuron model that includes both I_{NaP}-dependent (persistent sodium current) and I_{CAN}-dependent (calcium dynamics and CAN current) burst-generating

mechanisms. The DB solutions in this case are related to those analyzed previously in a model that included the CAN current[30] but not persistent sodium. In the earlier work, the passage of a trajectory across a fast subsystem SNIC bifurcation curve induced burst onset, as in parabolic bursting. The depolarization block emerged when the trajectory passed through a fast subsystem Andronov–Hopf (AH) bifurcation curve and ended when a second crossing of the AH curve occurred, which resulted in additional spikes being fired before the active phase finally terminated via a second crossing of the SNIC curve. In our analysis, the onset of DB bursting occurs at a fast subsystem fold bifurcation, as in square-wave bursting. The approach to the depolarization block occurs via passage through a SNPO bifurcation, which is followed by a passage through an AH bifurcation (Fig. 3). In this case, a delayed bifurcation effect prevents a return to spiking after the AH bifurcation is crossed; when the delay wears off, the only fast subsystem attractor available corresponds to the hyperpolarized rest state, and thus burst termination occurs, although the way-in/way-out analysis of the timing of this transition is beyond the scope of this work.

In other neural settings,[20,37,38,41] authors have studied a bursting pattern that they called pseudo-plateau bursting, in which the jump to the active phase is followed by damped oscillations as the trajectory approaches a stable branch of fast subsystem high-voltage equilibria. The DB bursting that arises here can feature an extended spiking period before passage through an SNPO bifurcation, but the part of the solution corresponding to the actual depolarization block is again associated with passage along a stable equilibrium branch. Interestingly, although we sometimes observe a bifurcation delay effect before the transition from oscillations to depolarization blocks, the transition is quite abrupt when it happens; explaining this abruptness remains as an open research direction.

We do not need to distinguish three timescales to obtain the mixed bursting solutions in this paper, a result that is consistent with our past analysis showing that even in a three-timescale version of the pre-BötC neuron model, variables do not need to be grouped into three separate timescale classes to produce mixed bursting patterns.[42] Importantly, to explain the pre-BötC model dynamics as thoroughly as we do, we go beyond a straightforward fast–slow decomposition. Indeed, the timescale of the intracellular calcium concentration falls between the fast timescales of the membrane potential and the potassium activation/sodium inactivation $[(V,n)]$ and the common slower timescale of the persistent sodium inactivation, total calcium concentration, and IP_3 activation variables (h, Ca_{tot}, l). Nonetheless, it turns out to be useful to consider intracellular calcium together with persistent sodium inactivation in some instances and together with total calcium and IP_3 activation in others. The latter view has a biological underpinning, in that intracellular calcium, total calcium, and IP_3 activation all represent calcium-related variables and appear in a structurally different way than the voltage and gating variables in the model. These observations contribute to recent trends in the literature to explore issues that lie outside of traditional fast–slow decomposition analysis, such as what happens when individual variables evolve on different timescales in different regions of the phase space.[16] In our analysis, competition between rates of change of different variables determines which bifurcation curves are crossed, and hence some key aspects of dynamics arise in periods when separation of timescales is in flux. The development of rigorous approaches to such scenarios represents an interesting challenge for future consideration.

In the broader context of respiratory neurodynamics, a final important point is that, within the intact neural circuit for respiration, the role of the intrinsic bursting capabilities of pre-BötC neurons has still not been determined. Recent results strongly support the importance of the CAN current for generating adequate motor outputs to achieve breathing.[13,23,25] Experimental results on persistent sodium current are less definitive, with different findings arising in different experimental conditions.[12,21,24] It is possible that synaptic interactions among pre-BötC neurons critically impact their contributions to respiration;[5,10,26,30] these interactions are outside of the scope of this paper, and studying synaptic coupling among pre-BötC neurons with complicated burst patterns could represent an interesting future research direction, building on past work on this topic.[2,29,32] It is also possible that the inputs to pre-BötC neurons in the intact respiratory circuit push these neurons out of the regime in which they would be able to generate intrinsic bursts; interestingly, even if this is the case, the currents that support intrinsic bursting at other input levels may still contribute to the network dynamics in subtle but important ways.[24,31]

ACKNOWLEDGMENTS

J. E. Rubin was partially supported by the National Science Foundation (NSF) under Award No. DMS 1612913. This research was supported in part by the NSF (Grant No. DMS 1440386) to the Mathematical Biosciences Institute. The authors thank Christopher Del Negro for reading and commenting on an earlier version of this manuscript.

APPENDIX: NONDIMENSIONALIZATION

From numerical simulations of system (1), we find that the membrane potential V typically lies between -60 mV and 20 mV. Correspondingly, we define $T_x = \max(1/\tau_x(V))$ over the range $V \in [-60, 10]$ mV and then define $t_x(V)$, a rescaled version of $\tau_x(V)$, by $t_x(V) = T_x\tau_x(V)$, where $x \in \{n, h\}$. We also define g_{max} to be the maximum of the six gating conductances $g_{NaP}, g_{Na}, g_K, g_{Ca}, g_{CAN}, g_{leak}$.

To nondimensionalize Ca_i and Ca_{tot}, we let $G(Ca_i) = \frac{[IP_3]Ca_i}{([IP_3]+K_I)(Ca_i+K_d)}$, $G_{SERCA}(Ca_i) = \frac{V_{SERCA}Ca_i}{K_{SERCA}^2+Ca_i^2}$, and $G_{PMCA}(Ca_i) = \frac{V_{PMCA}Ca_i}{K_{PMCA}^2+Ca_i^2}$. From numerical simulations, Ca_i and Ca_{tot} typically lie between 0 μM and 1 μM. Therefore, we define $G_c = \max(G^3(Ca_i))$, $G_s = \max(G_{SERCA}(Ca_i))$, and $G_p = \max(G_{PMCA}(Ca_i))$ over the range $Ca_i \in [0, 1]\,\mu$M, and let $P_{max} = \max\{L_{IP_3}, P_{IP_3}G_c, G_s\}$. We then define the rescaled versions of J_{ERin}, J_{ERout}, J_{PMin}, J_{PMout} from Eq. (4) by $\bar{J}_{ERin} = \frac{J_{ERin}\sigma}{P_{max}Q_c}$, $\bar{J}_{ERout} = \frac{J_{ERout}\sigma}{P_{max}Q_c}$, $\bar{J}_{PMin} = \frac{J_{PMin}}{\alpha g_{Ca}Q_v}$, and $\bar{J}_{PMout} = \frac{J_{PMout}}{G_pQ_c}$. We can, therefore, rewrite the calcium dynamics as

$$\frac{dCa_i}{dt} = \frac{f_i}{V_i\lambda}(\alpha g_{ca}Q_v\bar{J}_{PMin} - G_pQ_c\bar{J}_{PMout}) + \frac{f_iP_{max}Q_c}{V_i\sigma}(\bar{J}_{ERin} - \bar{J}_{ERout}),$$
$$\frac{dCa_{tot}}{dt} = \frac{f_i}{V_i\lambda}(\alpha g_{ca}Q_v\bar{J}_{PMin} - G_pQ_c\bar{J}_{PMout}). \quad \text{(A1)}$$

From (1), we obtain the following equivalent system:

$$\begin{aligned}
\frac{C_m}{Q_t g_{\max}}\frac{dv}{d\tau} &= -\bar{I}_{\mathrm{NaP}} - \bar{I}_{\mathrm{Na}} - \bar{I}_{\mathrm{K}} - \bar{I}_{\mathrm{Ca}} - \bar{I}_{\mathrm{CAN}} - \bar{I}_{\mathrm{leak}},\\
\frac{1}{Q_t T_n}\frac{dn}{d\tau} &= (n_\infty(v) - n)/t_n,\\
\frac{1}{Q_t T_h}\frac{dh}{d\tau} &= (h_\infty(v) - h)/t_h,\\
\frac{V_i\sigma}{Q_t f_i P_{\max}}\frac{dca_i}{d\tau} &= \left(\frac{\sigma\alpha g_{\mathrm{ca}} Q_v}{P_{\max}\lambda Q_c}\bar{J}_{\mathrm{PMin}} - \frac{\sigma G_p}{P_{\max}\lambda}\bar{J}_{\mathrm{PMout}}\right) + (\bar{J}_{\mathrm{ERin}} - \bar{J}_{\mathrm{ERout}}),\\
\frac{V_i\lambda}{Q_t f_i G_p}\frac{dc_{tot}}{d\tau} &= \left(\frac{\alpha g_{\mathrm{ca}} Q_v}{G_p Q_c}\bar{J}_{\mathrm{PMin}} - \bar{J}_{\mathrm{PMout}}\right),\\
\frac{1}{Q_t Q_c A}\frac{dl}{d\tau} &= \bar{K}_d(1-l) - ca_i l,
\end{aligned} \tag{A2}$$

with dimensionless currents $\bar{I}_y = I_y/(g_{\max} Q_v)$.

Since we expect $V \in [-60, 10]$ mV and Ca_i, $Ca_{\mathrm{tot}} \in [0, 1]\,\mu$M, suitable choices for the voltage and calcium scales are $Q_v = 100$ mV and $Q_c = 1\,\mu$M. For the choice of parameters specified in Table I, we have $g_{\max} = g_{\mathrm{Na}} = 28$ nS given that $g_{\mathrm{NaP}}, g_{\mathrm{CAN}}$ are smaller than g_{Na}. The numerical evaluation of $1/\tau_n(V)$ and $1/\tau_h(V)$ over $V \in [-60, 10]$ shows that $T_n \approx 6.5\,\mathrm{ms}^{-1}$ and $T_h \approx 0.001$–0.0165 /ms. We also compute $G_c \approx 0.0456$, $G_s \approx 1,000$ /ms, and $G_p \approx 3.3$ /ms; therefore, we have $P_{\max} \approx 1412$ /ms.

Direct calculations show that all terms on the right-hand side of (A2) are bounded by 1. The coefficients of the derivatives on the left-hand sides, therefore, reveal the relative rates of evolution of the variables. We find that $C_m/g_{\max} = 0.75$ ms, $1/T_n \approx 0.15$ ms, $1/T_h \approx 60.5$–1000 ms, $V_i\sigma/(f_i P_{\max}) \approx 5.24$ ms, $V_i\lambda/(f_i G_p) \approx 485$ ms, and $1/(Q_c A) = 2000$ ms. We choose our reference time to be $Q_t = 1$ ms and set

$$\begin{aligned}
R_v &=: \frac{C_m}{Q_t g_{\max}} \sim O(1), \quad R_n =: \frac{1}{Q_t T_n} \sim O(0.1),\\
R_h &=: \frac{1}{Q_t T_h} \sim O(1000), \quad R_c =: \frac{V_i\sigma}{Q_t f_i P_{\max}} \sim O(10),\\
R_{c_{tot}} &=: \frac{V_i\lambda}{Q_t f_i G_p} \sim O(1000), \quad R_l =: \frac{1}{Q_t Q_c A} \sim O(1000).
\end{aligned} \tag{A3}$$

As a result, the dimensionless system (A2) becomes the system (5) given in Sec. II, namely,

$$\begin{aligned}
R_v\frac{dv}{d\tau} &= -\bar{I}_{\mathrm{NaP}} - \bar{I}_{\mathrm{Na}} - \bar{I}_{\mathrm{K}} - \bar{I}_{\mathrm{Ca}} - \bar{I}_{\mathrm{CAN}} - \bar{I}_{\mathrm{leak}} =: f_1(v, n, h, c),\\
R_n\frac{dn}{d\tau} &= (n_\infty(v) - n)/t_n(v) =: g_1(v, n),\\
R_h\frac{dh}{d\tau} &= (h_\infty(v) - h)/t_h(v) =: h_1(v, h),\\
R_c\frac{dca_i}{d\tau} &= \left(\frac{\sigma\alpha g_{\mathrm{ca}} Q_v}{P_{\max}\lambda Q_c}\bar{J}_{\mathrm{PMin}} - \frac{\sigma G_p}{P_{\max}\lambda}\bar{J}_{\mathrm{PMout}}\right) + (\bar{J}_{\mathrm{ERin}} - \bar{J}_{\mathrm{ERout}})]\\
&=: f_2(v, c, c_{tot}, l),\\
R_{c_{tot}}\frac{dc_{tot}}{d\tau} &= \left(\frac{\alpha g_{\mathrm{ca}} Q_v}{G_p Q_c}\bar{J}_{\mathrm{PMin}} - \bar{J}_{\mathrm{PMout}}\right) =: g_2(v, c),\\
R_l\frac{dl}{d\tau} &= \bar{K}_d(1-l) - ca_i l =: h_2(c, l).
\end{aligned} \tag{A4}$$

REFERENCES

[1] B. J. Bacak, J. Segaran, and Y. I. Molkov, "Modeling the effects of extracellular potassium on bursting properties in pre-Bötzinger complex neurons," J. Comput. Neurosci. **40**(2), 231–245 (2016).
[2] J. Best, A. Borisyuk, J. Rubin, D. Terman, and M. Wechselberger, "The dynamic range of bursting in a model respiratory pacemaker network," SIAM J. Appl. Dyn. Syst. **4**(4), 1107–1139 (2005).
[3] R. J. Butera, J. Rinzel, and J. C. Smith, "Models of respiratory rhythm generation in the pre-Bötzinger complex. I. Bursting pacemaker neurons," J. Neurophysiol. **82**(1), 382–397 (1999).
[4] M. Chevalier, N. Toporikova, J. Simmers, and M. Thoby-Brisson, "Development of pacemaker properties and rhythmogenic mechanisms in the mouse embryonic respiratory network," Elife **5**, e16125 (2016).
[5] C. A. Del Negro, G. D. Funk, and J. L. Feldman, "Breathing matters," Nat. Rev. Neurosci. **19**, 351–367 (2018).
[6] M. Diener, "The canard unchained or how fast/slow dynamical systems bifurcate," Math. Intelligencer **6**(3), 38–49 (1984).
[7] J. Drover, J. Rubin, J. Su, and B. Ermentrout, "Analysis of a canard mechanism by which excitatory synaptic coupling can synchronize neurons at low firing frequencies," SIAM J. Appl. Math. **65**(1), 69–92 (2004).
[8] J. R. Dunmyre, C. A. Del Negro, and J. E. Rubin, "Interactions of persistent sodium and calcium-activated nonspecific cationic currents yield dynamically distinct bursting regimes in a model of respiratory neurons," J. Comput. Neurosci. **31**(2), 305–328 (2011).
[9] G. B. Ermentrout and D. H. Terman, *Mathematical Foundation of Neuroscience* (Springer, New York, 2010).
[10] J. L. Feldman and C. A. Del Negro, "Looking for inspiration: New perspectives on respiratory rhythm," Nat. Rev. Neurosci. **7**, 232–241 (2006).
[11] P. E. Jasinski, Y. I. Molkov, N. A. Shevtsova, J. C. Smith, and I. A. Rybak, "Sodium and calcium mechanisms of rhythmic bursting in excitatory neural networks of the pre-Bötzinger complex: A computational modelling study," Eur. J. Neurosci. **37**, 212–230 (2013).
[12] H. Koizumi and J. C. Smith, "Persistent Na^+ and K^+-dominated leak currents contribute to respiratory rhythm generation in the pre-Bötzinger complex in vitro," J. Neurosci. **28**, 1773–1785 (2008).
[13] H. Koizumi, T. T. John, J. X. Chia, M. F. Tariq, R. S. Phillips, B. Mosher, Y. Chen, R. Thompson, R. Zhang, N. Koshiya, and J. C. Smith, "Transient receptor potential channels TRPM4 and TRPC3 critically contribute to respiratory motor pattern formation but not rhythmogenesis in rodent brainstem circuits," eNeuro **5**, 1 (2018).
[14] V. I. Krinskiĭ and IuM. Kokoz, "Analysis of the equations of excitable membranes. I. Reduction of the Hodgkin-Huxley equations to a 2D order system," Biofizika **18**, 506 (1973).
[15] B. G. Lindsey, I. A. Rybak, and J. C. Smith, "Computational models and emergent properties of respiratory neural networks," Comprehensive Physiol. **2**(3), 1619–1670 (2012).
[16] I. Lizarraga and M. Wechselberger, "Computational singular perturbation method for nonstandard slow-fast systems," arXiv:1906.06049 (2019).
[17] Y. I. Molkov, J. E. Rubin, I. A. Rybak, and J. C. Smith, "Computational models of the neural control of breathing," Wiley Interdiscip. Rev.: Syst. Biol. Med. **9**(2), e1371 (2017).
[18] A. I. Neishtadt, "Prolongation of the loss of stability in the case of dynamic bifurcations. I," . Differ. Equ. **23**, 1385–1390 (1987).
[19] A. I. Neishtadt, "Prolongation of the loss of stability in the case of dynamic bifurcations. II," Differ. Equ. **24**, 171–176 (1988).
[20] H. Osinga and K. Tsaneva-Atanasova, "Dynamics of plateau bursting depending on the location of its equilibrium," J. Neuroendocrinol. **22**, 1301–1314 (2010).

[21]R. W. Pace, D. D. Mackay, J. L. Feldman, and C. A. Del Negro, "Role of persistent sodium current in mouse preBötzinger complex neurons and respiratory rhythm generation," J. Phys. (Lond.) **580**, 485–496 (2007).
[22]C. Park and J. E. Rubin, "Cooperation of intrinsic bursting and calcium oscillations underlying activity patterns of model pre-Bötzinger complex neurons," J. Comput. Neurosci. **34**, 345–366 (2013).
[23]R. S. Phillips, T. T. John, H. Koizumi, Y. I. Molkov, and J. C. Smith, "Biophysical mechanisms in the mammalian respiratory oscillator re-examined with a new data-driven computational model," eLife **8**, e41555 (2019).
[24]R. S. Phillips and J. E. Rubin, "Effects of persistent sodium current blockade in respiratory circuits depend on the pharmacological mechanism of action and network dynamics," PLoS Comput. Biol. **15**, e1006938 (2019).
[25]M. C. D. Picardo, Y. K. Sugimura, K. E. Dorst, P. S. Kallurkar, V. T. Akins, X. Ma, R. Teruyama, R. Guinamard, K. Kam, M. S. Saha, and C. A. Del Negro, "TRPM4 ion channels in pre-Bötzinger complex interneurons are essential for breathing motor pattern but not rhythm," PLoS Biol. **17**, e2006094 (2019).
[26]J. C. Rekling and J. L. Feldman, "PreBötzinger complex and pacemaker neurons: Hypothesized site and kernel for respiratory rhythm generation," Ann. Rev. Physiol. **60**, 385–405 (1998).
[27]J. Rinzel, "Excitation dynamics: Insights from simplified membrane models," Fed. Proc. **44**, 2944–2946 (1985).
[28]J. Rinzel, *A Formal Classification of Bursting Mechanisms in Excitable Systems*, Mathematical Topics in Population Biology, Morphogenesis and Neurosciences (Springer, Berlin, 1987), pp. 267–281.
[29]K. L. Roberts, J. E. Rubin, and M. Wechselberger, "Averaging, folded singularities, and torus canards: Explaining transitions between bursting and spiking in a coupled neuron model," SIAM J. Appl. Dyn. Syst. **14**, 1808–44 (2015).
[30]J. E. Rubin, J. A. Hayes, J. L. Mendenhall, and C. A. Del Negro, "Calcium-activated nonspecific cation current and synaptic depression promote network-dependent burst oscillations," Proc. Natl. Acad. Sci. USA **106**, 2939–2944 (2009).
[31]J. E. Rubin and J. C. Smith, "Robustness of respiratory rhythm generation across dynamic regimes," PLoS Comput. Biol. **15**, e1006860 (2019).
[32]J. Rubin and D. Terman, "Synchronized activity and loss of synchrony among heterogeneous conditional oscillators," SIAM J. Appl. Dyn. Syst. **1**, 146–174 (2002).
[33]I. A. Rybak, N. A. Shevtsova, K. Ptak, and D. R. McCrimmon, "Intrinsic bursting activity in the pre-Bötzinger complex: Role of persistent sodium and potassium currents," Biol. Cybern. **90**(1), 59–74 (2004).
[34]L. P. Shilnikov, A. Shilnikov, D. Turaev, and L. Chua, *Methods of Qualitative Theory in Nonlinear Dynamics* (World Scientific, 2010), Parts I and II
[35]J. Smith, H. Ellenberger, K. Ballanyi, D. Richter, and J. Feldman, "Pre-Bötzinger complex: A brainstem region that may generate respiratory rhythm in mammals," Science **254**(5032), 726–729 (1991).
[36]J. C. Smith, A. P. Abdala, I. A. Rybak, and J. F. Paton, "Structural and functional architecture of respiratory networks in the mammalian brainstem," Phil. Trans. Roy. Soc. B: Biol. Sci. **364**(1529), 2577–2587 (2009).
[37]W. Teka, J. Tabak, T. Vo, M. Wechselberger, and R. Bertram, "The dynamics underlying pseudo-plateau bursting in a pituitary cell model," J. Math. Neurosci. **1**(1), 12 (2011).
[38]W. Teka, K. Tsaneva-Atanasova, R. Bertram, and J. Tabak, "From plateau to pseudo-plateau bursting: Making the transition," Bull Math Biol. **73**(6), 1292–1311 (2011).
[39]N. Toporikova and R. Butera, "Two types of independent bursting mechanisms in inspiratory neurons: An integrative model," J. Comput. Neurosci. **30**(3), 515–528 (2011).
[40]N. Toporikova, M. Chevalier, and M. Thoby-Brisson, "Sigh and eupnea rhythmogenesis involve distinct interconnected subpopulations: A combined computational and experimental study," eNeuro **2**(2), 11 (2015).
[41]K. Tsaneva-Atanasova, A. Sherman, F. van Goor, and S. Stojilkovic, "Mechanism of spontaneous and receptor-controlled electrical activity in pituitary somatotrophs: Experiments and theory," J. Neurophysiol. **98**(1), 131–144 (2007).
[42]Y. Wang and J. Rubin, "Multiple timescale mixed bursting dynamics in a respiratory neuron model," J. Comput. Neurosci. **41**(3), 245–268 (2016).
[43]Y. Wang and J. Rubin, "Timescales and mechanisms of sigh-like bursting and spiking in models of rhythmic respiratory neurons," J. Math. Neurosci. **7**(1), 3 (2017).